

**Product Development Team  
for  
NEXRAD Enhancements**

**Quarterly Report – 4<sup>th</sup> Quarter FY 01**

**01.6.1 Damaging Winds**

*Development and enhancement of the Damaging Downburst Detection and Prediction Algorithm (DDPDA) to ensure that it meets the aviation communities' needs for the prediction and detection of damaging winds associated with both wet and dry atmospheric environments, along with larger scale downbursts.*

a) Current Efforts

DDPDA work during FY 2001 focused on updating and correcting data in the NSSL damaging wind events database, creating improved downburst prediction equations, and finalizing code changes to the DDPDA.

The damaging wind event database was reanalyzed to eliminate storm cells that had been poorly identified by the Storm Cell Identification and Tracking (SCIT) algorithm. Earlier results had shown that about 1/3 of cells identified by SCIT and inserted into the data had serious errors in the time-height trend information. Since these data are used as input to the DDPDA, it was necessary to eliminate them so that the downburst prediction equations will be as accurate as possible. After eliminating the erroneous storm cells and adding new cases, there are a total of 100 severe wind events and 1349 non-severe cells from 64 event days and 15 different WSR-88D radars across the United States.

Recent improvement to SCIT algorithm routines that associate cell components in the vertical and storm cells in time will provide improvements to the time-height trends produced by the DDPDA. These trends are also used as input to the DDPDA downburst prediction equations, and should bring about an improvement the performance of the DDPDA.

Due to unforeseen technical difficulties with the software used to score the DDPDA's performance, the final set of downburst prediction equations and performance statistics are not yet available. These will be submitted as an addendum to this report by October 31, 2001.

b) Planned Efforts

The DDPDA task is complete upon submission of the final report.

c) Problems/Issues

None.

d) Interface with other Organizations

None.

e) Activity Schedule Changes

None.

**01.6.2 Polarization and Frequency Diversity**

*Continue development of algorithms that utilize polarization data to detect and predict the movement of the volumetric extent of hydrometeors such as hail, rain, snow, sleet, icing conditions, and freezing rain that are hazardous to aircraft.*

a) Current Efforts

**(NSSL):**

1) Planning for the Joint Polarization Experiment (JPOLE)

During the first week of October, NSSL hosted a series of planning meetings for the Joint Polarization Experiment (JPOLE). JPOLE will include the first operational test of weather radar polarimetry. In addition, a planned field phase of JPOLE will provide an opportunity to investigate many complementary scientific objectives.

In the first meeting, NSSL scientists and NWS representatives discussed the operational demonstration phase of the experiment. A representative from the FAA also attended this meeting. Issues addressed included data collection schedules, operational demonstration goals, product needs, evaluation requirements, and interactions with operational forecasters. Many of the real-time, polarimetric hydrometeor classification products currently provided to the Norman, Oklahoma NWS office (such as hail detection, rain/snow discrimination, and bird identification) also address core FAA needs.

In the second meeting, several government and university scientists, along with representatives from the FAA, NWS, and DOD, discussed preliminary plans for a proposed JPOLE intense observation period (IOP). During the IOP, plans are being made to collect multi-seasonal verification sets that will be used to conduct a detailed investigation of polarimetric WSR-88D data quality. The verification data sets will also be used to investigate numerous scientific objectives. One of the goals of the cold-season phase of the IOP will be to collect combined Ka and S-band polarimetric radar data sets, a comparison of which can be used to assess the usefulness of polarimetric WSR-88D radar data for iden-

tifying cloud particle (including cloud water) types. Work is continuing to identify field facilities and secure additional funding for this field phase of the experiment.

In the third meeting, NSSL and NCAR scientists met with FAA representatives to review current research, discuss plans for JPOLE, and prioritize future FAA needs. Preliminary plans were also made to conduct a workshop at the May 2002 PMR in Boulder, Colorado.

## 2) Calibration of polarimetric radar data

Many operational WSR-88D radars in the US experience radar beam blockage problems at lower elevation scans. Blockage can easily be detected if the radar beam is blocked completely and no radar data are available from certain azimuthal sectors. However, if beam blockage is partial (which is a more common situation), then corresponding biases in radar reflectivity factor might go undetected for years. This adversely affects overall radar performance. For example, a negative bias of 1 dB results in 25% underestimation of rainfall. The situation becomes even worse when the error due to blockage is combined with additional bias due to radar transmitter/receiver miscalibration.

The radar reflectivity factor ( $Z$ ), measured by the NSSL's Cimarron polarimetric radar, was found to be significantly biased due to partial blockage of the radar beam at the lowest elevation angle  $0.5^\circ$ , which is likely caused by nearby trees and a ridge to the south of the radar. This bias varies with azimuth and changes with time depending on the state of foliage on the trees, atmospheric refraction, etc. Beam blockage affects differential reflectivity ( $ZDR$ ) as well.

A novel technique based on consistency of  $Z$ ,  $ZDR$ , and specific differential phase  $KDP$  (which is not affected by blockage) has been developed at NSSL. The technique can be used to make corrections for radar miscalibration and beam blockage in both the  $Z$  and  $ZDR$  data.

Fig. 1 illustrates the dependencies of the  $Z$  and  $ZDR$  biases in the azimuthal sector  $180 - 225^\circ$  (where effect of blockage is most pronounced) for the rain event on October 21, 2000. The curve for the  $Z$  bias is in good agreement with the results of direct comparisons of radar reflectivities measured with the Cimarron and KTLX WSR-88D radar. Fig. 1 shows that reflectivities measured by the Cimarron radar were 5 to 12 dB (depending on the azimuth) lower than the ones obtained from the reference radar. The  $ZDR$  bias varies between -0.6 and -0.1 dB.

The polarimetric calibration technique can also be used to deduce possible miscalibration of the operational KTLX radar. Fig. 2 displays biases in areal rainfall estimates for different methods as a function of hour of observation, ranked in the chronological order. A dense network of 42 rain gauges was used for

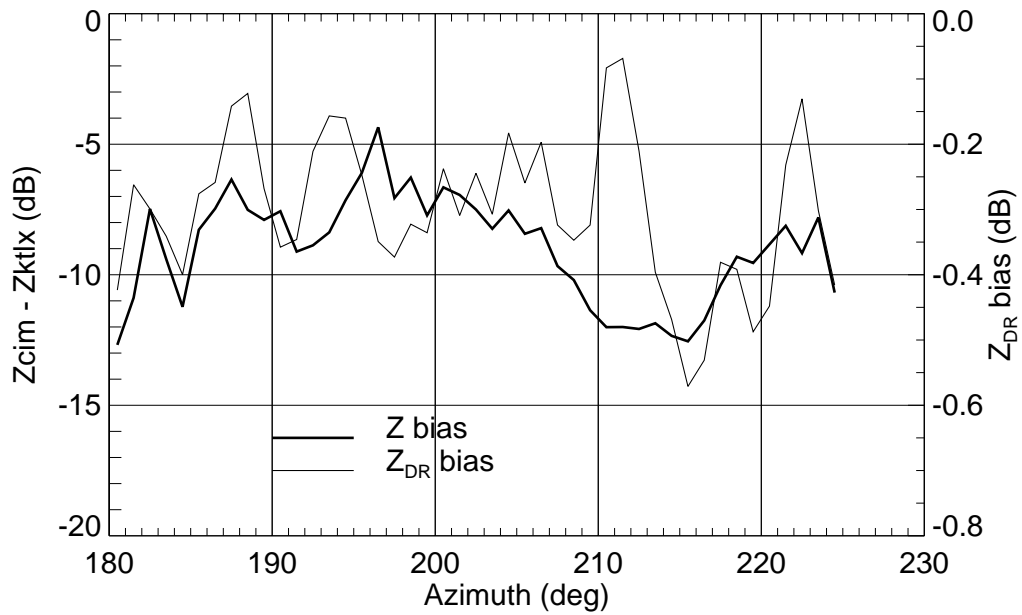


Figure 1. Azimuthal dependencies of the Z and ZDR biases due to radar beam blockage in the sector containing nearby trees and a ridge.

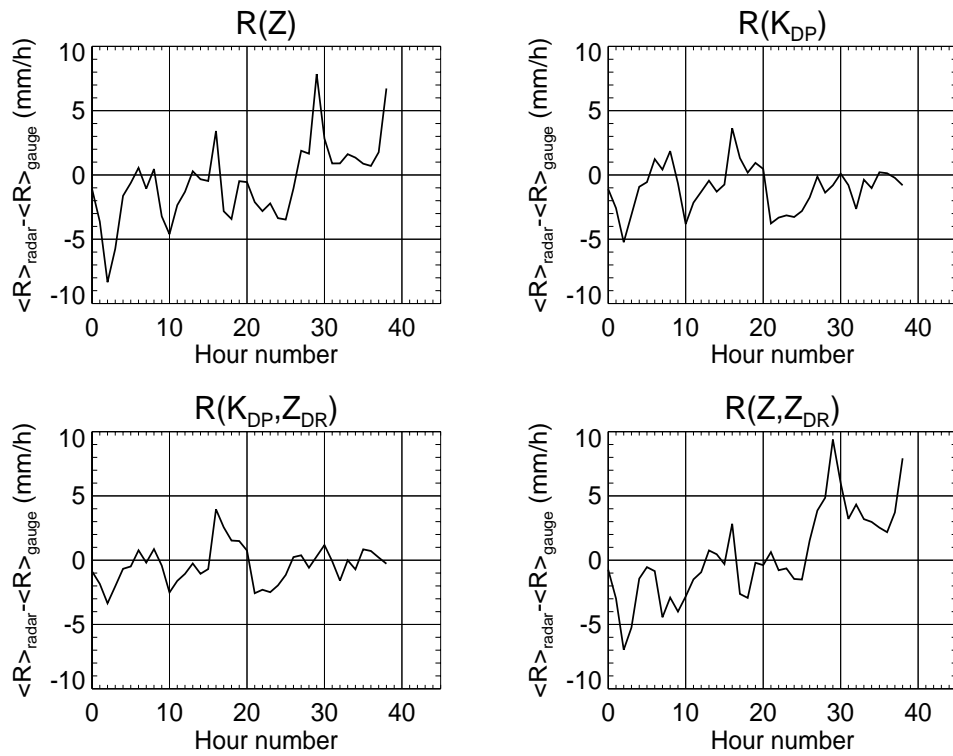


Figure 2. The difference between areal mean rain rates obtained from the radar and gauges for 39 hours of observations during 13 rain events computed for various rainfall estimation algorithms.

ground validation of different rainfall algorithms. The first hour of observation dates back to 23 September 1997, whereas the last hour (out of total 39) corresponds to the 23 February 2001 rain event. Radar reflectivities  $Z$  measured with the WSR-88D radar and KDP and ZDR obtained from the polarimetric radar were used for computation of rain accumulations.

An obvious temporal trend in the error for the  $Z$ -based estimates might indicate miscalibration of the operational WSR-88D radar that slowly progresses with time. No such trend is evident for the KDP-based algorithms.

See the attached preprint from the 18th American Meteorology Society Interactive Information and Processing Systems Conference preprint for more in-depth information on JPOLE progress and plans.

**(NCAR):** See the attached white paper "Polarization Algorithm Development: Case Studies" for full details on NCAR activities.

#### b) Planned Efforts

NSSL: Work continues to improve the real-time Hydrometeor Classification Algorithm (HCA) that is being delivered to operational forecasters at the Norman, Oklahoma NWS office. Within the next two months, a cold-season hydrometeor classification scheme (currently under development) will be introduced. Other engineering and software improvements have resulted in improved transmission speed and eliminated data losses.

In the past few weeks, NSSL has also procured a workstation that will allow NSSL scientists to locally view the HCA display in real time. This ability is crucial for making real-time algorithm adjustments and for evaluating algorithm performance. Polarimetric radar data (from the NSSL Cimarron polarimetric radar, to be switched to data from the polarimetric WSR-88D radar in the spring of 2002) recorded for each event are used for more in depth analyses of algorithm performance. Over the course of the past summer, several good hail storm cases have been collected. Additionally, NSSL hopes to collect several good cold-season precipitation cases starting this fall.

NCAR: There is a continuing need to verify the retrieved microphysical properties and hydrometeor designations and to determine which classifications are justifiable and practical. A proposal for twenty hours of flight time has been submitted to the National Science Foundation for in situ hydrometeor data collection in conjunction with the International H<sub>2</sub>O Project (IHOP-2002). Another possibility is the planned Joint Polarimetric Experiment (JPOLE) to be conducted in Oklahoma in 2003. See the attached white paper "Polarization Algorithm Development: Case Studies" for full details.

d) Interface with other Organizations

None.

e) Activity Schedule Changes

None.

**01.6.3 Circulations**

*Continue to enhance NSSL's Mesocyclone Detection and Tornado Detection Algorithms (MDA, TDA) while developing in parallel a new algorithm which combines MDA and TDA into one algorithm which detects and analyzes all circulations - the Vortex Detection and Diagnosis Algorithm (VDDA).*

a) Current Efforts

The enhanced neural net equations for MDA and TDA are complete. See the attached report "Bayesian Neural Networks for MDA and TDA" for full details.

b) Planned Efforts

This completes the neural net efforts and the milestone defined in the TD.

c) Problems/Issues

None.

d) Interface with other Organizations

None.

e) Activity Schedule Changes

None.

**01.6.4 Technical Facilitation**

*Continue to work through the process of algorithm transition to the operational WSR-88D system. This also includes development of a Common Operations Development Environment (CODE) and Application Programmer Interfaces (API's) for a more rapid integration of algorithms into the operational system.*

a) Current Efforts

The WDSS2 system was enhanced in several ways to support various research efforts at NSSL and to implement new visualization techniques.

1. More work was done on visualizing dual polarization data, particularly in terms of speed, continuing the work done during the last quarter.

2. Legends, configurability and documentation was added to the single radar 3D visualization. This visualization can now be done on the fly either over the entire radar domain or using just a single storm. The 3D volume can be shown superimposed on a single radar elevation image.

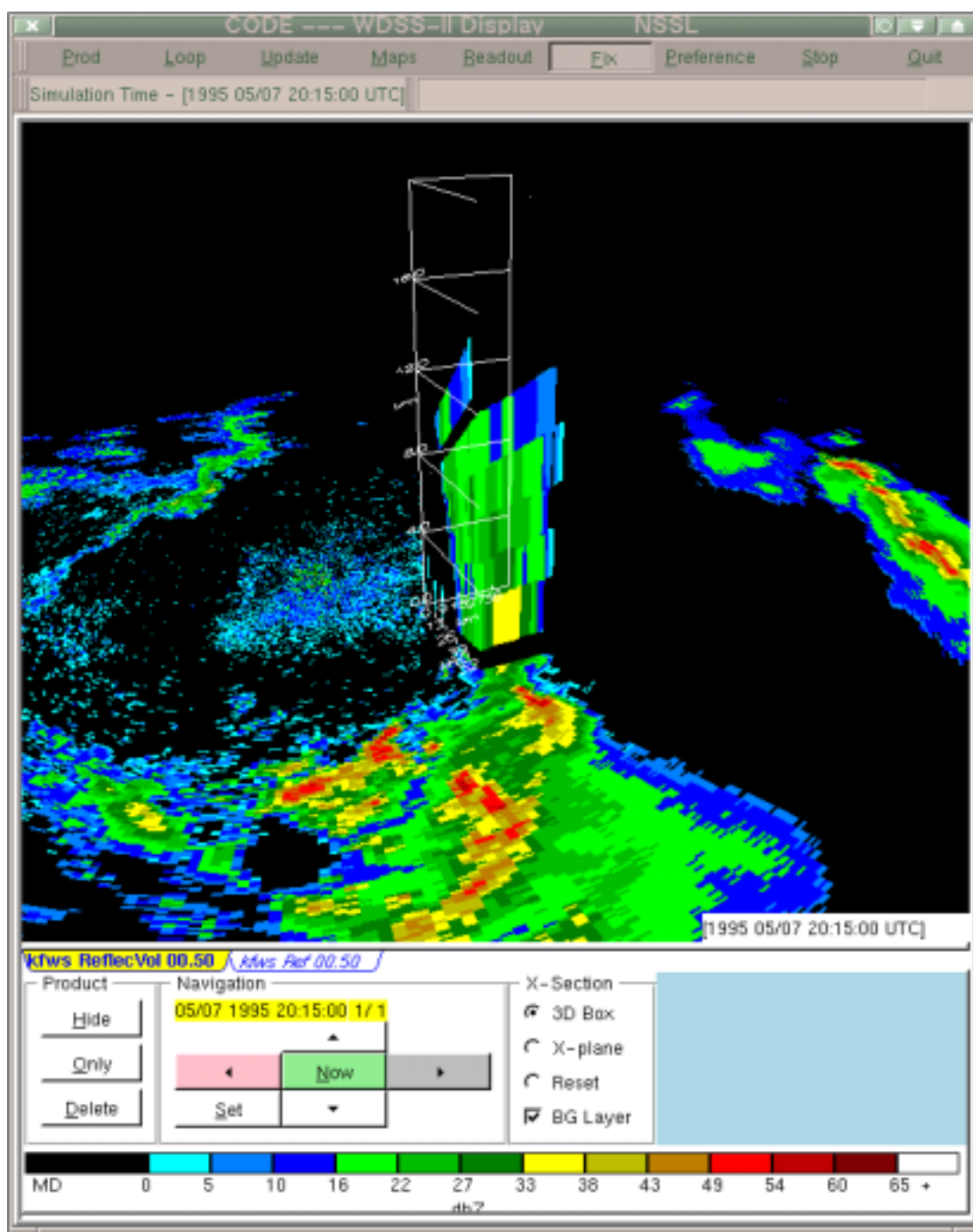


Figure 3. 3D perspective volume shown superimposed on a single radar elevation image.

3. It is now possible to extract a high resolution vertical cross-section by flying through a storm. The cross-section is referenced by color maps, axes labeling, etc.

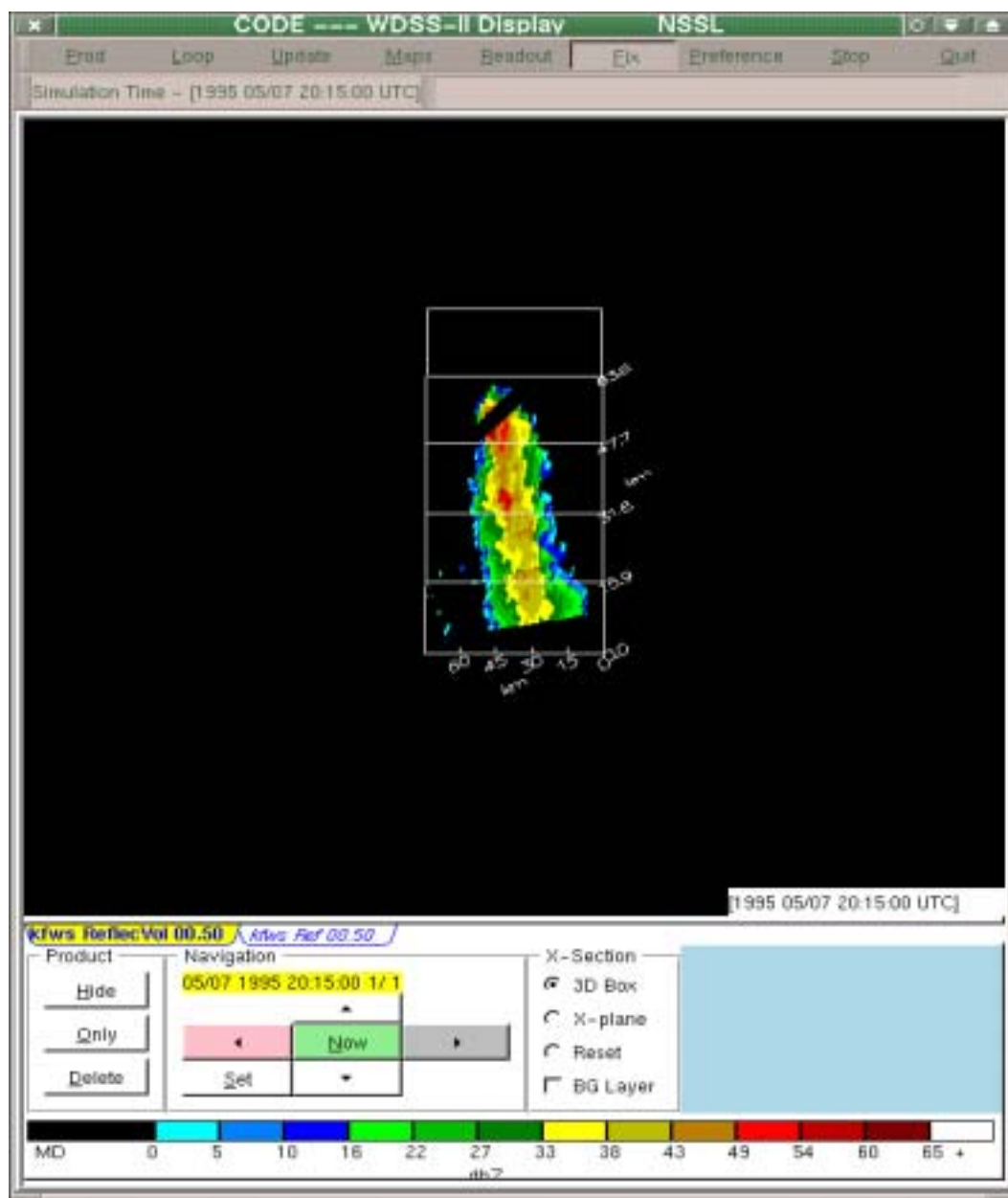


Figure 4. Vertical cross-section from WDSS-II with configurable positional referencing.

4. It is possible to step forward and backward through radar *virtual* volumes that are constantly updated.

The buttons are color-coded to indicate which times are present (gray to indicate that the volume is not yet available, red to indicated that the volume is old,



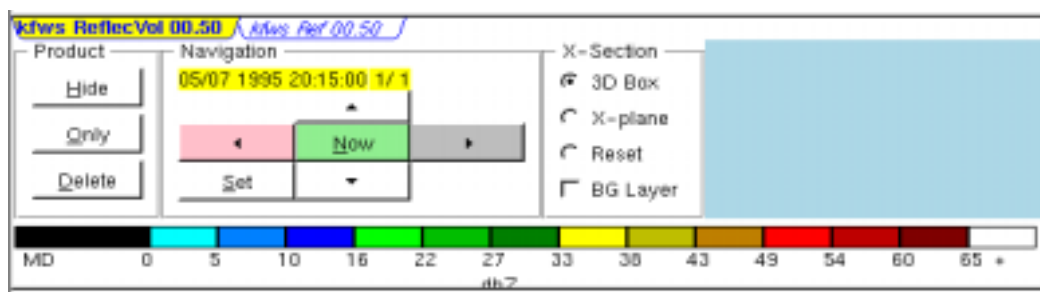


Figure 5. New WDSS-II navigational interface.

green to indicate that current data is available). We are currently working on the capability to be able to step and down in the virtual volume.

5. Tables, trends and tracks of any algorithm can be obtained.

RowName	Azimuth	Range	Circ	Burst	SVRH	HailSize	POH	VIL	MXZ	Hgt
2	357	61.3	TVS		60%	2.25	100%	53	50	5.5
86	7	60.5	TVS		50%	1.75	100%	24	54	7.6
100	327	35.1	TVSMes		0%	0.00	0%	2	37	5.1
7	338	38.3	Meso		70%	1.75	100%	64	58	7.8
93	53	44.4	Meso		40%	1.75	100%	22	55	5.2
1	48	48.0	CPLT		30%	1.50	100%	42	56	2.7
36	176	55.1	Circ		40%	1.75	100%	40	55	1.5
4	341	72.5	Circ		30%	1.75	100%	23	54	4.6

Figure 6. Output table for severe storm algorithms.

6. The K-Means clustering algorithm was implemented on infrared satellite data (11um) and the display was implemented in WDSS-II. K-Means clustering will also prove useful to radar data as it will result in more stable tracking for storms and so more stable algorithm output and performance.

7. Terrain can be visualized in conjunction with weather data.

8. The ability to read in mesonet data was implemented. We are now integrating it with other data sources into the system.

#### b) Planned Efforts

Continue development of advanced algorithm display and verification tools.

#### c) Problems/Issues

None.

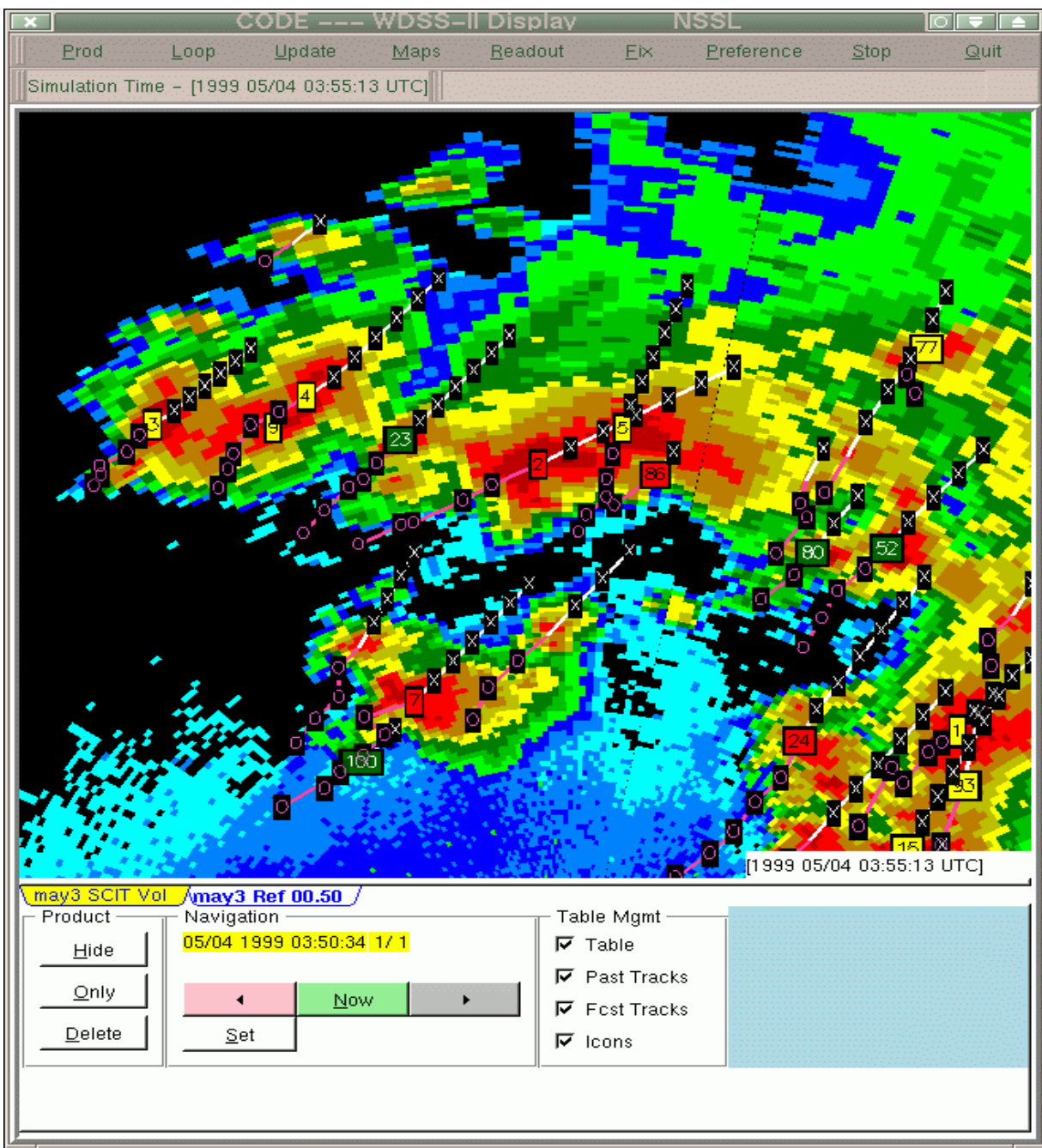


Figure 7. Output tracks, configurable to track any algorithm output.

d) Interface with other Organizations

None.

e) Activity Schedule Changes

None.

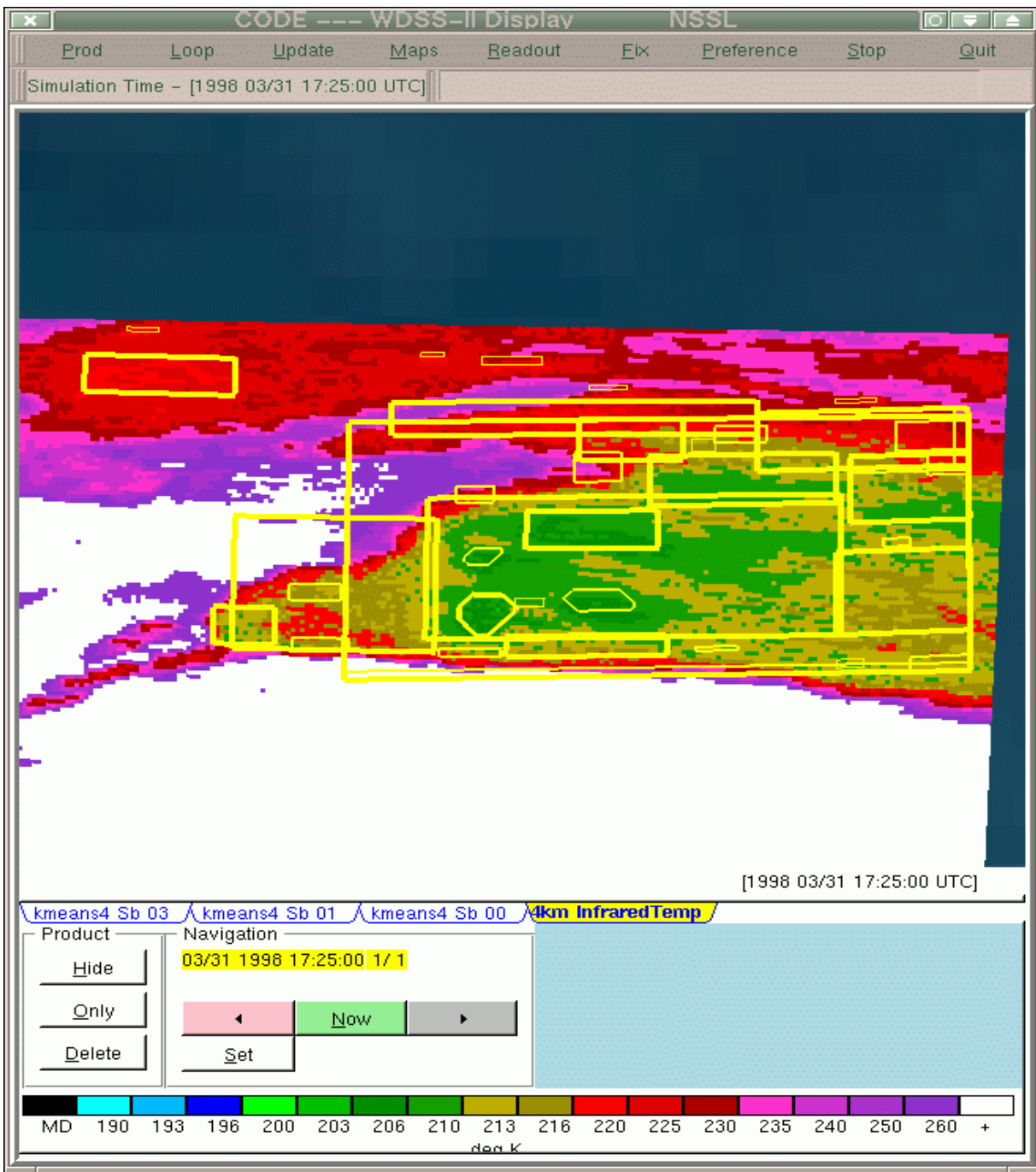


Figure 8. Various entities from infrared satellite data identified and tracked using K-means clustering. Each entity is contained within a polygon, and embedded polygons represent nested K-means cluster thresholds.

#### 01.6.6 Rapid Update

*Develop software that produces algorithm output after each tilt, thus providing immediate information to the users.*

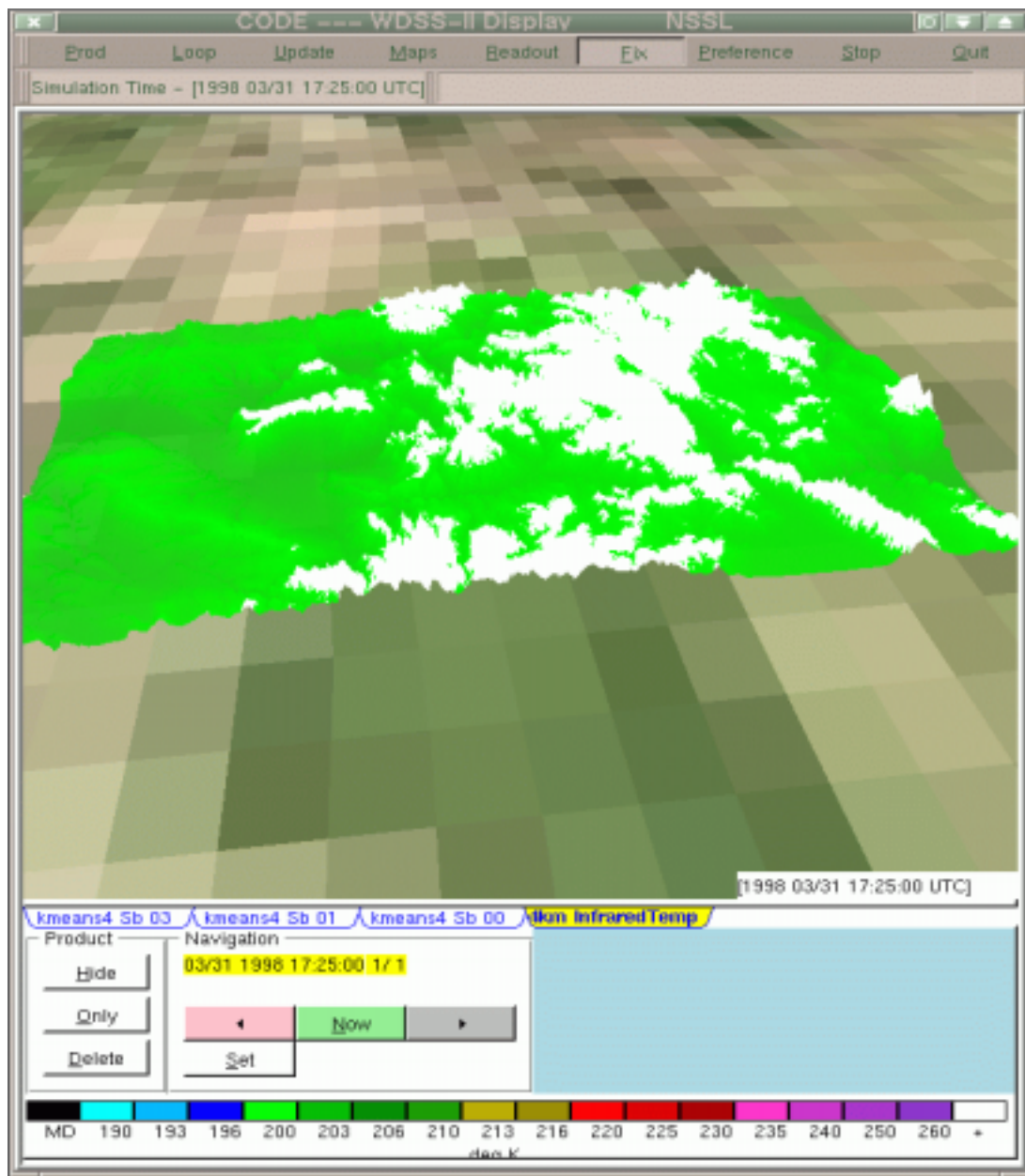


Figure 9. High-resolution terrain map overlaid atop a low resolution terrain.

#### a) Current Efforts

Real-time testing is complete. However, hardware issues have plagued the Rapid Update debugging effort. In addition, various technical issues dealing with graphics and varying compiler versions from system to system have prevented any substantive headway.

b) Planned Efforts

Complete debugging and implementation will be complete by 30 November 2001.

d) Interface with other Organizations

None.

e) Activity Schedule Changes

Delayed implementation to 30 November 2001.

**01.6.7 Cell and Area Tracking**

*Integration of the Storm Cell Identification and Tracking (SCIT), the Correlation Tracking (CT) and Scale Separation (SS) algorithms into a single multi-scale precipitation tracking and forecast package.*

a) Current Efforts

MIT/LL provided NSSL with GDST version 5.1b late in the final month of this quarter, along with supporting libraries. Software engineering efforts were focused on getting the GDST to run in real time within the WDSS-II system, and also incorporating the latest version of GDST into the WDSS-II system. The late delivery of the GDST libraries has created minor delays the Final Report. The report will be complete by 31 October.

b) Planned Efforts

Completion of the report completes the SS/CT task.

c) Problems/Issues

None.

d) Interface with other Organizations

None.

e) Activity Schedule Changes

None.

**01.6.9 Composite Products**

*Develop high resolution radar layer products that are rapidly updated.*

#### a) Current Efforts

The activities for this quarter include the continued work with the Mitre on prototype uses of the 3D reflectivity mosaic in the DSR (Display System Replacement) environment. The latest 3D mosaic data and a decoder program were sent to the Mitre. The NSSL 3D reflectivity mosaic has been compared with the WARP (Weather And Radar Processor) reflectivity mosaic. It is shown that the NSSL mosaic has high spatial resolution and an improved AP/GC removal (Kelley, 2001, personal communication).

A new product, brightband height field, is also provided to the Mitre. An experimental icing display is tested in the DSR system. Hazardous icing tends to occur in regions with temperature between 0°C and -25°C that contain high concentrations of supercooled liquid water. The brightband top height represents the 0°C level very well (<http://www.nssl.noaa.gov/wrd/wish/qpe/bbid/index.htm>). The 3D reflectivity mosaic fields can show regions of clouds and precipitation where high concentration of liquid water exists. Based on these two fields, an initial icing display is developed for the DSR. Around each radar, regions within a 3 km layer above the radar-detected brightband and with reflectivity above a certain threshold are considered risky areas for potential icing.

Task 01.6.9 is complete for this fiscal year. Documentation for the AP/GC removal scheme and the bright band identification scheme can be found at <http://www.nssl.noaa.gov/wrd/wish/qpe/apremoval/index.htm> and <http://www.nssl.noaa.gov/wrd/wish/qpe/bbid/index.htm>, respectively. A PowerPoint presentation for the latest 3D reflectivity mosaic algorithm can be found at: <http://www.nssl.noaa.gov/wrd/wish/qpe/mosaic/index.htm> and a reference on the mosaic currently contained in a preprint from the 30th Radar Conference. The preprint is attached.

#### b) Planned Efforts

The activities through out the next quarter and beyond will include setting up a real-time 3D reflectivity mosaic for a FAA corridor. The mosaic will probably be generated on nested, multi-resolution grids. A coarse resolution grid will be used to show a broad picture of weather systems in the whole corridor. Several fine resolution grids will be setup near each NEXRAD sites within the corridor. The 3D reflectivity mosaic on the fine grids will provide detailed storm structures and can be used for further analyses and applications (e.g., by the Convective Weather PDT).

Brightband identification scheme and icing products will be further refined and improved using real-time RUC (20 km) model data.

c) Problems/Issues

None.

d) Interface with other Organizations

Worked with Mitre on the prototype uses of the 3D reflectivity mosaic and radar detected brightband information.

e) Activity Schedule Changes

None.

**01.6.11 Volume Coverage Patterns**

*Develop and implement Volume Coverage Patterns (VCP's) relevant to the goals of the AWR PDT's.*

a) Current Efforts

Data were collected using the NSSL's KOUN radar in combination with the legacy RPG at the Radar Operations Center (ROC). Minimal data were collected this quarter due to lack of appropriate weather events.

08/17/01 VCP 61

09/07/01 VCP's 45, 46.

All milestones for Task 01.6.11 are complete.

b) Planned Efforts

Continue analysis and data collection on new VCP's. In particular, check that current algorithms are compatible with new VCP's, and correct any incompatibilities.

c) Problems/Issues

None.

d) Interface with other Organizations

None.

e) Activity Schedule Changes

None

#### **01.6.12 Product Implementation**

*Explore and define implementation paths within the aviation community systems that are best for NEXRAD PDT products.*

##### a) Current Efforts

The in-flight Icing PDT, the Winter Weather PDT, and the convective Weather PDT are potential users of polarimetric radar products. These three PDTs will be contacted and invited to the NEPDT face time at the December AWRP PMR. They will also be invited to attend a JPOLE meeting to be held at the May 2002 PMR.

##### b) Planned Efforts

Continue evaluating the efficacy and appropriateness of NEPDT products.

##### c) Problems/Issues

None.

##### d) Interface with other Organizations

None.

##### e) Activity Schedule Changes

None

#### **01.6.14 Multi-radar Composites**

*Develop a vision for FAA use of high resolution, rapid update, composite products which are produced from the integration of multiple WSR-88Ds.*

##### a) Current Efforts

The activities for the current quarter include further investigation of possible ways of mosaicking radial (or, Doppler) velocity fields. It seems that for the first step, a mosaic of radial and azimuthal derivatives of the Doppler velocity field would be useful as well as feasible. Radial derivatives of the Doppler velocity field can depict fine scale convergence. Azimuthal shears can provide important information for diagnosing turbulent storms that are potentially hazardous to airplanes. While the mosaic of the radial velocity field itself is difficult due to its vector nature, the derivatives are more of scalar fields and mosaicking the derivatives would make better physical sense. Below is an outline for a primitive regional mosaic of radial velocity derivative fields.

1) Quality check radial velocity fields (including dealiasing, outlier removal, etc.)



2) Derive radial and azimuthal derivatives of the Doppler velocity fields for each radar in 3D polar grids.

3) Remap the derivative fields from polar grids onto a pre-specified 3D Cartesian grid that covers the region of interest (e.g., a FAA corridor). The 3D Cartesian grid would be the same as the one for the 3D reflectivity mosaic (see task 01.6.9).

4) Generate a 3D radar coverage map for the Cartesian grid. The map indicates at each grid point which radar provides the best coverage. The coverage map would be dynamically updated based on which radars are available in the real-time. Note that a weighted mean of radial velocity derivatives from different radars is not wanted in the mosaic, because the derivatives from different radars are not in the same radial or azimuthal direction.

5) Mosaic the remapped derivative fields on the Cartesian grid based on the coverage map.

In theory, the 3D mosaic of radial velocity derivative fields, together with the 3D reflectivity mosaic, would allow WSR-88D users and algorithm developers the benefit to use and develop a wide variety of products and displays that more fully depict the evolution and life cycle of storms than single radar products. Examples include more physically realistic horizontal or vertical cross-sections. Existing single radar algorithms, like those in the SSAP, could be transferred and expanded to utilize data from multiple radars and other environmental data to more accurately determine storm attributes. Gridded data can also be easily combined with information from other data sources such as satellite data, model analyses or forecast fields increasing its value in the overall forecast and warning process.

#### b) Planned Efforts

Development of initial code for the mosaic of radial velocity derivative fields and development of a few case studies will be performed. The example velocity mosaic data will be examined and evaluated.

#### c) Problems/Issues

None.

#### d) Interface with other Organizations

None.

#### e) Activity Schedule Changes

None.

#### **01.6.15 WARP Activities**

*Examine adaptable parameters associated with NEXRAD data algorithms in WARP and determine optimal settings according to location and season as appropriate.*

##### a) Current Efforts

NSSL has received training on Unisys algorithms developed to mitigate anomalous propagation, ground clutter, and interference patterns from WSR-88D Level III real-time data for the WARP program. The algorithm software has been given to NSSL so that algorithm evaluation can commence. The robustness of the AP/Ground Clutter mitigation schemes will be evaluated by varying algorithm adaptable parameters, geographic location of AP events, and the season in which the AP events occur.

A way to produce Level-III data has been developed so that a local data base for WARP algorithm evaluation can be developed. This will be needed since all of the data cases so far provided by Unisys so involve interference or bulls-eye problems and not weather-induced AP problems. Whether additional cases will be forthcoming is uncertain. My work in this now is to keep an eye on the 88D network to find real-time AP events.

##### b) Planned Efforts

The WSR-88D network will be monitored to find real-time AP events for the data base being developed.

##### c) Problems/Issues

None.

##### d) Interface with other Organizations

NCAR: Attempting to identify AP cases suitable for analysis.

##### e) Activity Schedule Changes

None.

Terry J. Schuur<sup>(1,2)</sup>, Robert C. Elvander<sup>(3)</sup>, John G. Simensky<sup>(3)</sup>, Richard A. Fulton<sup>(3)</sup>

<sup>(1)</sup>Cooperative Institute for Mesoscale Meteorological Studies, Norman, OK

<sup>(2)</sup>National Severe Storms Laboratory, Norman, OK

<sup>(3)</sup>National Weather Service, Silver Spring, MD

## 1. INTRODUCTION

The open systems development and polarimetric upgrade to the KOUN WSR-88D radar has been a tri-agency effort supported by the National Weather Service (NWS), Federal Aviation Administration (FAA), and Air Force Weather Agency (AFWA). As this work nears completion, plans are being made to conduct the Joint Polarization Experiment (JPOLE), which will include the first operational test of weather radar polarimetry. In addition, JPOLE will provide an opportunity to investigate many complementary hydrological and meteorological scientific objectives. This paper describes the goals and present plans for the JPOLE project.

## 2. JPOLE OVERVIEW

The overarching goals of JPOLE are to test the engineering design and determine the data quality of a polarimetric WSR-88D radar, demonstrate the utility and feasibility of the radar, and to collect data and information that will allow for a cost/benefit analysis to be performed. In July of 2000, an initial JPOLE planning meeting was held at the National Severe Storms Laboratory (NSSL) in Norman, Oklahoma. At that meeting, plans were made for an experiment that will essentially consist of two phases: a multi-seasonal test and evaluation period (using local facilities for the collection of verification data sets, to begin in the spring of 2002), and an intense observation period (using both local and community-wide facilities for the collection of verification data sets, to begin in the spring of 2003). The first phase will emphasize a demonstration of the utility of the polarimetric KOUN WSR-88D radar, and a test and evaluation of its engineering design and data quality. In addition, the second phase will address broad scientific objectives.

Since a long-term goal of JPOLE is to transfer polarimetric radar technology to an operational setting, plans were also made to begin introducing operational forecasters to polarimetric radar data and products prior to the start of KOUN WSR-88D polarimetric radar data collection. Over the past year, NSSL has therefore begun delivering real-time polarimetric radar data and products from the NSSL Cimarron radar (located approximately 40 km northwest of KOUN) to forecasters at the Norman, Oklahoma NWS Forecast Office. Plans

for the future development of these products will be presented in more detail later in this paper.

A second JPOLE planning meeting is scheduled for October of 2001 (after the submission deadline for this paper). In that meeting, efforts will be made to refine the operational requirements and scientific objectives (as listed here) and to begin making plans for the field phase portion of the experiment.

## 3. JPOLE OPERATIONAL DEMONSTRATION

The JPOLE operational demonstration objectives and requirements can be broken down into two broad categories: 1) evaluating the engineering design and data quality of a polarimetric WSR-88D radar, and 2) examining the benefits of polarimetric radar data to operational meteorologist, hydrologists, and aviation users.

### 3.1 Engineering Design and Data Quality

The operational demonstration will provide an opportunity to evaluate critical engineering and data quality issues. For example, radar data quality must be assessed through a detailed comparison with verification data sets, the radar scanning strategy evaluated to assess compatibility with requirements of the existing WSR-88D radar system, and the simultaneous transmission mode (Doviak et al., 2000) examined to calibrate polarimetric radar measurements, establish and verify engineering specifications, and investigate short and long term stability. More specifically, the engineering design and data quality objectives of the operational demonstration are to

- Demonstrate the accuracy of KOUN reflectivity, velocity, and spectrum width measurements through comparisons with conventional WSR-88D radar data
- Demonstrate the accuracy of KOUN polarimetric measurements through comparisons with high-quality research polarimetric radar data
- Demonstrate that polarimetric precipitation estimation and hydrometeor classification products can be collected with acceptable antenna rotation rates (all previous research results were obtained with relatively slow scan strategies)
- Perform tests to ensure minimal degradation in VCP times, and no degradation in ground clutter

---

*Corresponding author address:* Dr. Terry J. Schuur, National Severe Storms Laboratory, 1313 Halley Circle, Norman, OK, 73069; email: schuur@nssl.noaa.gov

filtering, anomalous propagation filtering, and velocity dealiasing

- Evaluate the value of alternate  $\rho_{HV}$  and  $L_{DR}$  scans (and limits to any of the variables)

### 3.2 Benefits to Operational Users

In addition to addressing engineering and data quality issues, JPOLE also seeks to examine the benefits of polarimetric radar data to operational meteorologist, hydrologists, and aviation users. This will be accomplished by conducting an evaluation of the performance of polarimetric radar rainfall and hydrometeor products. As such, operations during both field phases (covering both warm and cold season precipitation) will focus on the collection of data sets that can be used for a detailed comparison of conventional and polarimetric radar products. This evaluation will be completed both in 1) real-time with the collaboration of operational forecasters, and 2) post-analysis where a more detail analysis of polarimetric algorithm performance can be made. More specifically, the product performance evaluation objectives are to

- Improve Quantitative Precipitation Estimation (QPE)
- Use QPE to improve operational hydrologic forecasts (especially for flash flood events)
- Discriminate hail from rain and gauge hail size
- Identify precipitation type in winter storms (dry/wet snow, sleet, rain)
- Identify biological scatterers (and their effects on the wind measurements)
- Identify the presence of chaff (and its effect on precipitation measurements)
- Identify areas of ground clutter and anomalous propagation
- Provide improved initial conditions and constraints to numerical models for short term forecasts
- Investigate the feasibility of identifying aircraft icing conditions

Product comparisons will be of fundamental importance to the test and evaluation of the polarimetric KOUN WSR-88D radar's capabilities. As such, it is imperative that real-time data collection be conducted in collaboration with operational hydrologists, meteorologists, and aviation users, whose insight will be of vital importance to the evaluation of WSR-88D radar products.

## 4. PRODUCT DEVELOPMENT AND DELIVERY

In preparation for the full WSR-88D radar test, the NSSL began to introduce polarimetric radar data and products (from the polarimetric NSSL Cimarron radar) to forecasters at the Norman, Oklahoma NWS Forecast Office in the spring of 2001. As part of the NSSL Warning Decision Support System – Integrated Information (WDSS-II) software package, a polarimetric Hydrometeor Classification Algorithm (HCA) provided detailed information on the occurrence of severe hail,

location of anomalous propagation, and presence of biological (birds and insects) scatterers. Information on rain rate intensity was also provided by the algorithm.

An example of the HCA output from the spring 2001 operational test, as displayed by WDSS-II, is shown in Figure 1.

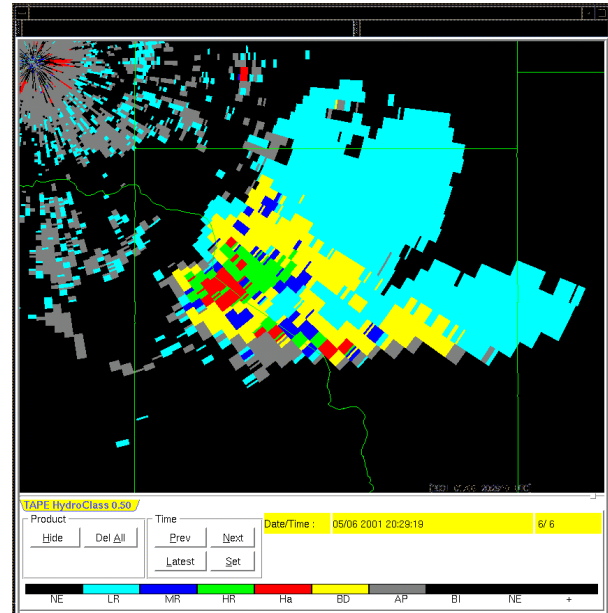


Fig. 1 WDSS-II Hydrometeor Classification Algorithm for the May 6, 2001 hail storm.

Figure 1 depicts the classification for a quasi-stationary, severe storm that produced 2 cm hail on May 6, 2001. The warm-season HCA categories shown in this figure are LR=light rain, MR=moderate rain, HR=heavy rain, Ha=hail, BD=big drops, AP=ground clutter and anomalous propagation, and BI=birds/insects. For this case, the HCA clearly depicts a large hail region surrounded by both heavy and moderate rainfall. A large region of rainfall wherein the drop size distribution is dominated by a deficit of small drops was also indicated by the HCA. These “big drop” regions, which can be attributed to drops that originate as melting hail aloft (and fall to ground while still containing ice cores) or the result of coalescence growth in the convective updraft (and fall to ground before significant drop breakup occurs) are characteristic of regions where radar-based rain rate is commonly overestimated. All fields showed remarkable temporal consistency from one sweep to the next.

During each precipitation event, NSSL scientists sat with NWS forecasters and assisted them in the use of the WDSS-II display and the interpretation of the polarimetric data and products. After each event, forecasters would fill out a short, web-based evaluation form. This information would then be used by scientists to improve algorithm performance and by software developers to improve WDSS-II functionality.

Future enhancements to this delivery/display system will include a classification package that will be better suited for classifying hydrometeor types in winter

precipitation events (such as snow, sleet, and freezing rain) and the addition algorithms that will focus on providing improved polarimetric precipitation accumulation estimates. Plans also call for switching the WDSS-II polarimetric data feed from the NSSL Cimarron radar to the KOUN WSR-88D radar in the spring of 2002.

## 5. JPOLE INTENSE OBSERVATION PERIOD

While JPOLE is primarily designed to be an operational demonstration project, the infrastructure provided by the operational test and evaluation requirements present a unique opportunity to also investigate several complementary hydrological and meteorological scientific objectives. In the spring of 2003, plans are therefore being made to conduct a more extensive JPOLE Intense Observation Period (IOP) in central Oklahoma. The primary goals of this IOP are to 1) collect dense, ground-based and airborne verification data sets that can be used to assess the KOUN radar data and product quality, and 2) collect high-quality, hydrological/meteorological data sets that can be used to investigate several scientific objectives, which are crucial towards advancing knowledge that will lead to future improvements of polarimetric radar algorithms. The JPOLE operational demonstration data collection will extend into the IOP. In turn, verification data sets collected as part of the IOP will be used to better assess the accuracy of the polarimetric KOUN WSR-88D radar data and products.

Since the first JPOLE planning meeting, scientists from a number of educational institutions and government agencies have submitted scientific objectives that are being combined into a JPOLE Science Overview Document. This document will serve as a template for the design and future operations plan of the JPOLE IOP. Preliminary plans call for the deployment of several ground-based and mobile facilities to central Oklahoma for the spring of 2003. These include, a research polarimetric radar that can be strategically placed in central Oklahoma to provide both a source of high-quality data that can be used for a comparison with the KOUN radar data (as well as provide input for hydrological distributed modeling studies), research aircraft to provide in situ microphysical data, and ground based rain gauge networks, disdrometers, and hail chase vehicles. More specific JPOLE IOP objectives are to

- Improve physical understanding of polarimetric signatures
- Collect data that can be used to evaluate the accuracy of operational precipitation and hydrometeor identification algorithms
- Investigate the effect of natural drop size distribution variability on conventional and polarimetric rainfall estimators
- Investigate the effect of drop oscillations and canting angles on conventional and polarimetric rainfall estimators

- Investigate how microphysical information derived from polarimetric radar measurements can be used in cloud resolving models
- Examine the microphysical basis for drop size distribution variability in both cold and warm season precipitation events
- Investigate how improved precipitation estimates from polarimetric rainfall measurements can be used to initialize hydrologic models.
- Measure streamflow and runoff and conduct hydrologic modeling studies
- Investigate how input data uncertainties influence flood prediction, the maximum time/space scales required to accurately simulate a flash flood, and the basin characteristics that are most important in transforming rainfall into runoff
- Assess how Ka-band (hydrometeor identification) and X-band (precipitation) measurements can be used to improve interpretation of polarimetric S-band radar data

## 6. SUMMARY

The Joint Polarization Experiment will represent the first operational test of the polarimetric KOUN WSR-88D radar. Data collection during JPOLE will be used to conduct detailed comparisons of conventional and polarimetric radar products, which will be of fundamental importance to the test and evaluation of the radar's capabilities. Additional facilities available during a proposed Intense Observation Period will provide much needed verification data sets that will allow for a detailed investigation of several hydrological and meteorological scientific objectives. Critical engineering and data quality issues will also be examined.

In preparation for JPOLE, the NSSL WDSS-II system has been used to deliver real-time polarimetric radar data and products from the NSSL Cimarron radar to forecasters at the Norman, Oklahoma NWS Office. Work is currently progressing to further coordinate real-time data collection with operational hydrologists, meteorologists, and aviation users, whose insight will be of vital importance to the evaluation of WSR-88D radar products.

## 7. REFERENCES

- Doviak, R. J., V. Bringi, A. Ryzhkov, A. Zahrai, and D. Zrnic, 2000: Considerations for polarimetric upgrades to operational WSR-88D radars. *J. Atmos. Oceanic Tech.*, **17**, 257-278.

**Polarization Algorithm Development:  
Case Studies**

Report Prepared for the Federal Aviation Administration

30 September 2001

Edward A. Brandes and Scott M. Ellis

National Center for Atmospheric Research  
P.O. Box 3000  
Boulder, CO 80307

Kim Elmore

National Severe Storms Laboratory  
1313 Halley Circle  
Norman, Oklahoma 73069

## 1. Introduction

Polarimetric radar measurements are sensitive to the size, shape, orientation, and composition of targets illuminated by the radar beam. The measurements can be used to discriminate among ground clutter echoes, range-folded echoes, biological scatterers, rain, mixed-phase precipitation, and various types of frozen hydrometeors. Algorithms are under development for hydrometeor discrimination, hail detection, and designation of the 0°C level. Exploratory studies are also being conducted to determine capabilities at S band for detecting icing hazards. For a tutorial on polarimetric radar measurements and prospects for new WSR-88D algorithms visit the NEXRAD Radar Operations Center (ROC) web site <http://www.osf.noaa.gov/app/sta/algorithm.htm> (2000 report).

This report describes some recent activities regarding the verification and testing of the hydrometeor classification algorithm (HCA) that runs in real time on NCAR's S-Pol radar (a brief description is given by Vivekanandan et al. 1999). Currently the algorithm makes designations in 17 categories, i.e., for insects, birds, ground clutter, and numerous meteorological classifications (including rainfall intensities, several hail categories, wet snow, and a number of ice crystal types). Here we demonstrate capabilities for detecting icing conditions and show preliminary results from an exploratory study to determine the distribution of particle types and sizes within thunderstorms. Ultimately the information gained on storm microphysical properties and hydrometeor distributions should lead to improved detection of weather hazards and improved parameterizations in numerical forecast models.

## 2. Aircraft Icing

Icing situations encountered during several recent field programs involving S-Pol and storm-penetrating aircraft are being investigated. Although not a panacea, there clearly is benefit for detecting some icing conditions. Hazard designation is facilitated in part by the capability of polarimetric radars to determine the 0°C (melting) level within precipitation and thereby designate potential icing layers.

Figure 1 shows a vertical cross-section through two small convective showers observed in Florida on 14 September 1998 during the PRECIP98 field program. The University of North Dakota's Citation penetrated the convective towers at the ! 10°C level and encountered supercooled liquid drops (SLDs). Individual panels in the figure show radar reflectivity ( $Z$ ), differential reflectivity ( $Z_{DR}$ ), linear depolarization ratio (LDR), the correlation coefficient between reflectivities at horizontal and vertical polarization ( $\rho_{HV}$ ), and particle designations made with the hydrometeor classification algorithm. Also shown are the melting level (as determined from the polarimetric measurements), some labeled hydrometeor classifications, and sample PMS images of particles observed by the aircraft. The aircraft location is indicated by a small black square. At the time of data collection both liquid drops and frozen particles were observed. The Rosemount icing probe indicated icing. From the suite of radar measurements, supercooled liquid (SL), light rain, wet snow, and a graupelSrain mixture were all inferred at and slightly above the aircraft's altitude.

Ellis et al. (2001) presented some examples from the Mesoscale Alpine Experiment conducted in Italy during the fall of 1999. An example of a light icing event that occurred on 20 September 1999 is reproduced in Fig. 2. The icing occurred at a temperature of ! 15°C in the uppermost portions of a precipitation layer. The figure shows a matched timeSspace series of aircraft observations and radar

measurements. There were two periods of icing. In Region I the reflectivity is low (averaging  $-0$  dBZ) suggesting that the median size of the particles is small. The differential reflectivity ( $Z_{DR}$ ) varies from  $0$  to  $1$  dB an indication that ice crystals are present. [Drizzle would have a  $Z_{DR}$  of  $0$  dB.] The correlation coefficient is significantly less than  $1.0$  suggesting the presence of mixed-phase hydrometeors (riming and potential icing conditions). Region II is characterized by reflectivity generally  $> 10$  dBZ,  $Z_{DR}$  is near  $0$  dB, and  $\rho_{HV}$  is close to  $1.0$ . In Region II the radar measurements are dominated by fairly-large irregular ice crystals with near spherical shapes in the mean which obscure the icing signatures.

### 3. Retrieval of Thunderstorm Microphysical Properties

Figure 3 presents radar measurements and retrieved microphysical parameters in a reconstructed cross-section through a thunderstorm that was observed on 22 September 1998 during PRECIP98. The retrieved parameters are obtained using the technique described by Zhang et al. (2001). Individual panels show radar reflectivity (DZ in dBZ, using the notation in the figure), differential reflectivity (ZDR, dB), total drop concentration (NT,  $m^{-3} mm^{-1}$ ), shape factor of the gamma drop-size distribution (MU), rain rate (RR,  $mm h^{-1}$ ), and the drop median volume diameter (D0, mm). The gamma distribution is given by

$$N(D) = N_0 D^\mu \exp(-\lambda D)$$

where  $N_0$  is a concentration parameter,  $\mu$  is a shape factor, and  $\lambda$  is a slope term. The distribution is exponential when  $\mu = 0$  and becomes more peaked (monodispersed) as  $\mu$  increases.  $N(D)$  can be integrated, with an appropriate upper size limit  $D_{max}$ , to find the total drop concentration. One half the liquid water content is contained in droplets smaller and one half in drops larger than the median volume diameter  $D_0$ , i.e.,

$$\int_0^{D_0} D^3 N(D) dD = \int_{D_0}^{D_{max}} D^3 N(D) dD$$

The rain rate has been computed with

$$R = \int_0^{D_{max}} D^3 N(D) v_t(D) dD$$

where  $v_t(D)$  is the raindrop terminal velocity. Particle designations made with the hydrometeor classification algorithm are shown in Fig. 4.

Inspection of the cross-sections reveals that the  $0^\circ C$  level is  $\sim 4.5$  km, except in the stronger convection where it rises to about  $5.5$  km. The HCA designations indicate that raindrops mixed with graupel may exist in updrafts to heights of  $6$  to  $7$  km. Except for a few spurious designations, hail is not indicated below the freezing level. Figure 3 affirms the strong correlation between drop size and radar reflectivity. Heavy rain areas tend to be characterized by small shape and slope parameters, i.e., the DSDs tend to be more exponential than in storm fringe areas where drop sizes are more narrowly



distributed (e.g., near a range of 47 km). The melting layer is characterized by wet snow or a rain/dry snow interface. At upper levels dry snow is inferred in the storm interior, and irregular ice crystals are implied at the storm's edges. By fully exploiting the capabilities of polarimetric radars for retrieving hydrometeor types and designating particle distributions, basic understanding of precipitation processes should increase.

#### 4. Discussion

There are a number of issues related to the development of a hydrometeor classification algorithm. There is a continuing need to verify the retrieved microphysical properties and hydrometeor designations and to determine which classifications are justifiable and practical. A proposal for twenty hours of flight time has been submitted to the National Science Foundation for in situ hydrometeor data collection in conjunction with the International H<sub>2</sub>O Project (IHOP-2002). Another possibility is the planned Joint Polarimetric Experiment (JPOLE) to be conducted in Oklahoma in 2003. Hopefully a storm-penetrating aircraft will be available. cursory examination of Figs. 1 and 4 reveals a number of spurious HCA designations and a relatively high "noise" level. Potential improvements being investigated are increased filtering (consistent with resolvable meteorological scales) and making the designations on a Cartesian grid to facilitate continuity checks. A committee of users and algorithm developers should be established to guide the HCA effort.

*Acknowledgment.* The drop-size distribution work reported here is supported by funds from the National Science Foundation that have been designated for the U.S. Weather Research Program at NCAR.

#### REFERENCES

- Ellis, S. M., J. Vivekanandan, S. Goeke, E. A. Brandes, J. Stith, R. J. Keeler, 2001: In-situ verification of remote aircraft icing detection using S-band polarization radar measurements. Preprints, *30th International Conf. on Radar Meteor.*, Amer. Meteor. Soc., Munich, Germany, 168-170.
- Vivekanandan, J., D. S. Zrnic, S. M. Ellis, R. Oye, A. V. Ryzhkov, and J. Straka, 1999: Cloud microphysics retrieval using S-band dual-polarization measurements. *Bull. Amer. Meteor. Soc.*, **80**, 381-388.
- Zhang, G., J. Vivekanandan, and E. Brandes, 2001: A method for estimating rain rate and drop size distribution from polarimetric radar measurements. *IEEE Trans. Geosci. Remote Sensing*, **39**, 830-841.

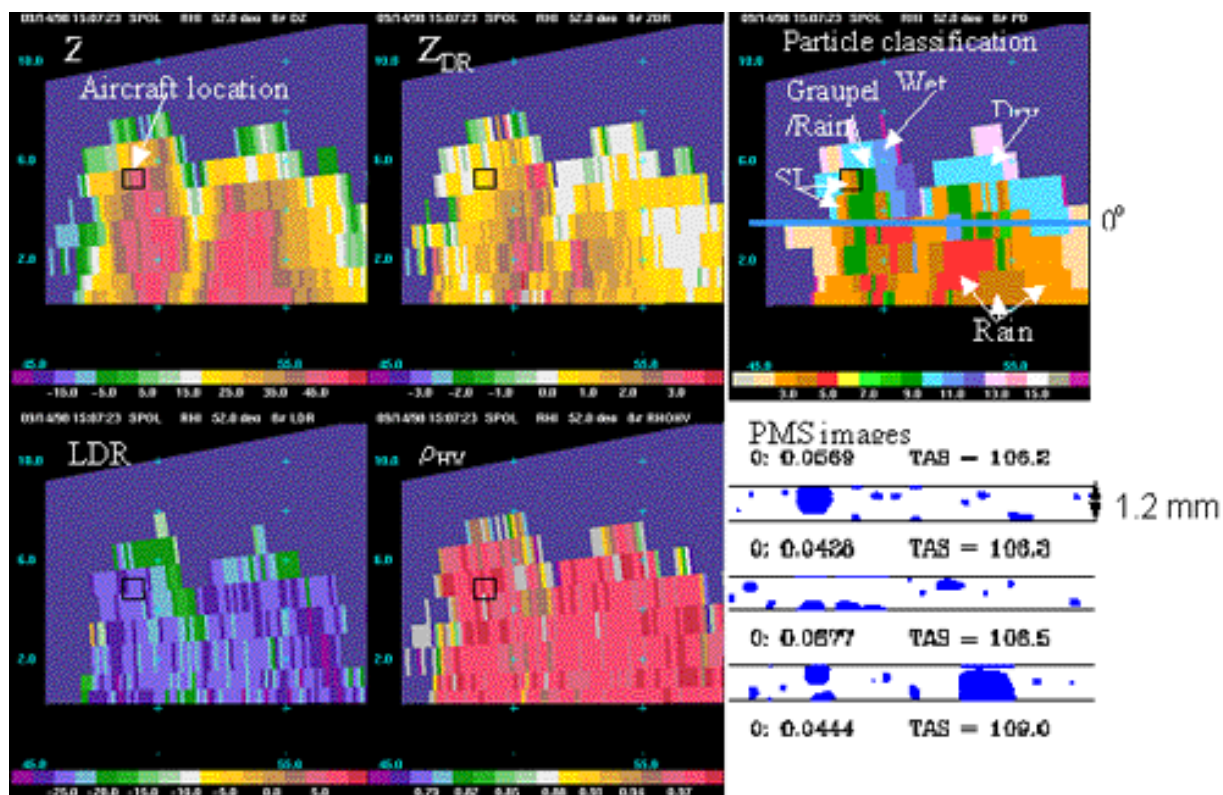


Fig. 1: A vertical cross-section through two small convective showers. Panels show radar reflectivity ( $Z$ ), differential reflectivity ( $Z_{DR}$ ), linear depolarization ratio (LDR), correlation coefficient ( $\rho_{HV}$ ), particle classifications, and images of observed hydrometeors.

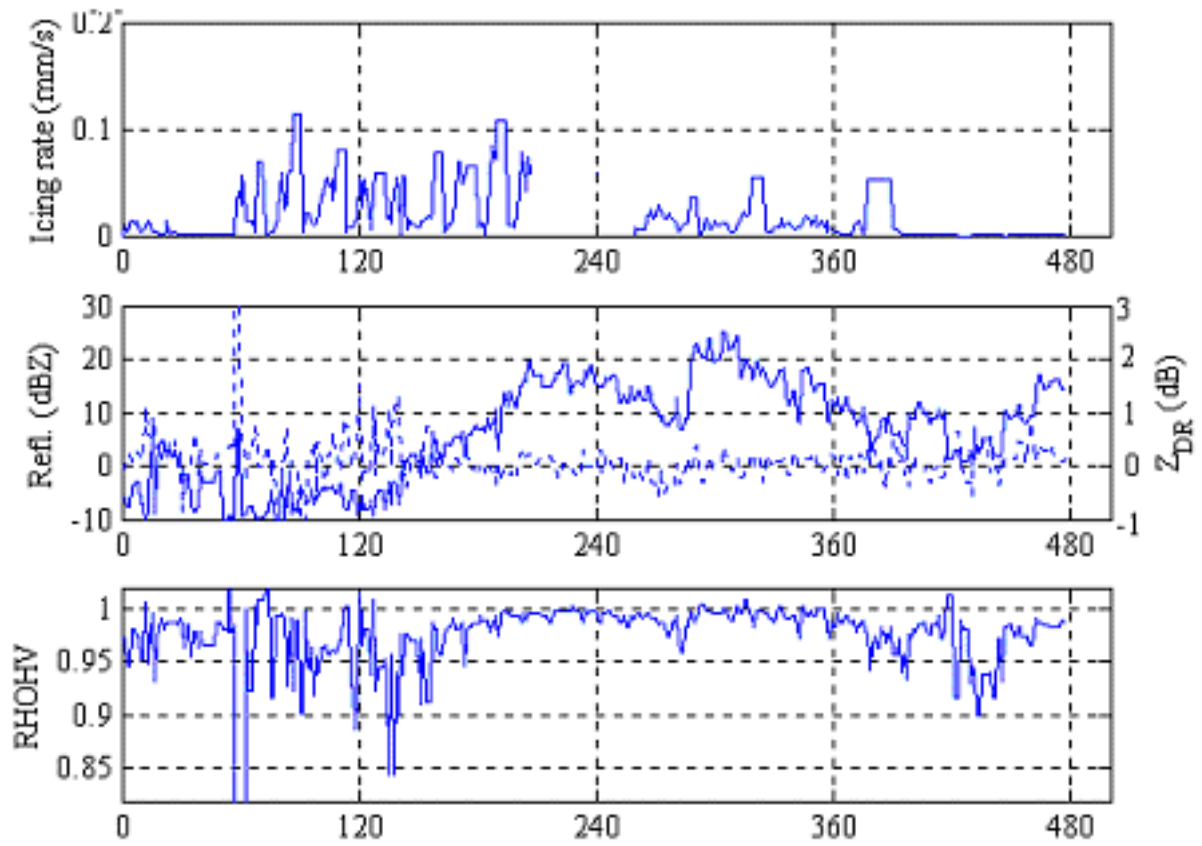


Fig. 2: A timeSspace series of radar and aircraft measurements. Radar reflectivity (Refl.) is shown with a solid line; differential reflectivity ( $Z_{DR}$ ) is dashed. RHOHV is the correlation coefficient.

# DSD Retrieval : 22 September 1998, 1956 UTC

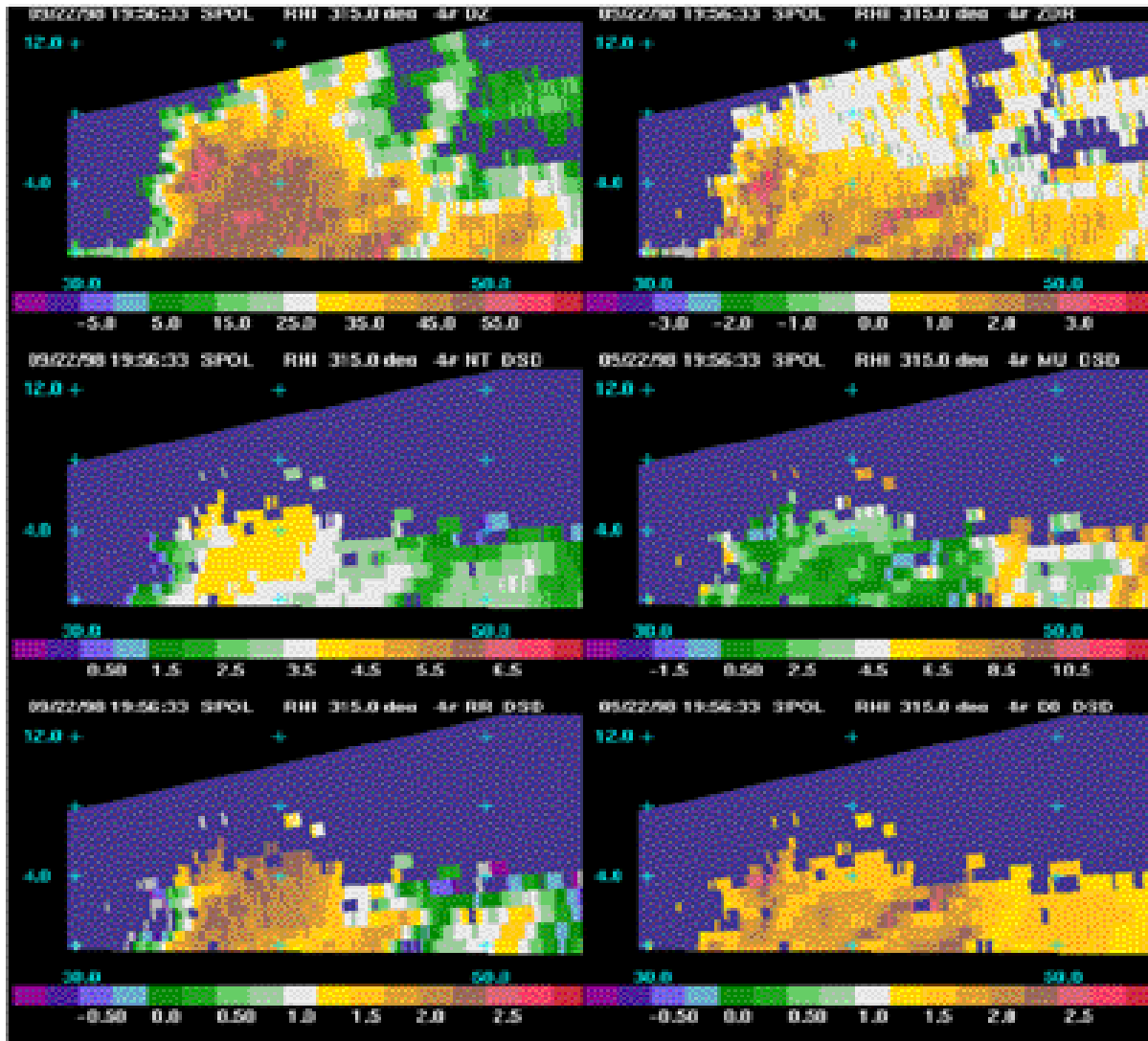


Fig. 3: A vertical cross-section through a thunderstorm showing radar reflectivity (DZ, dBZ), differential reflectivity (ZDR, dB), the logarithm of the total drop concentration (NT), the drop-size distribution shape factor (MU), the logarithm of the rain rate (RR, mm h<sup>-1</sup>), and the median drop diameter (D0), mm).

# Hydrometeor Classifications : 22 September 1998, 1956 UTC

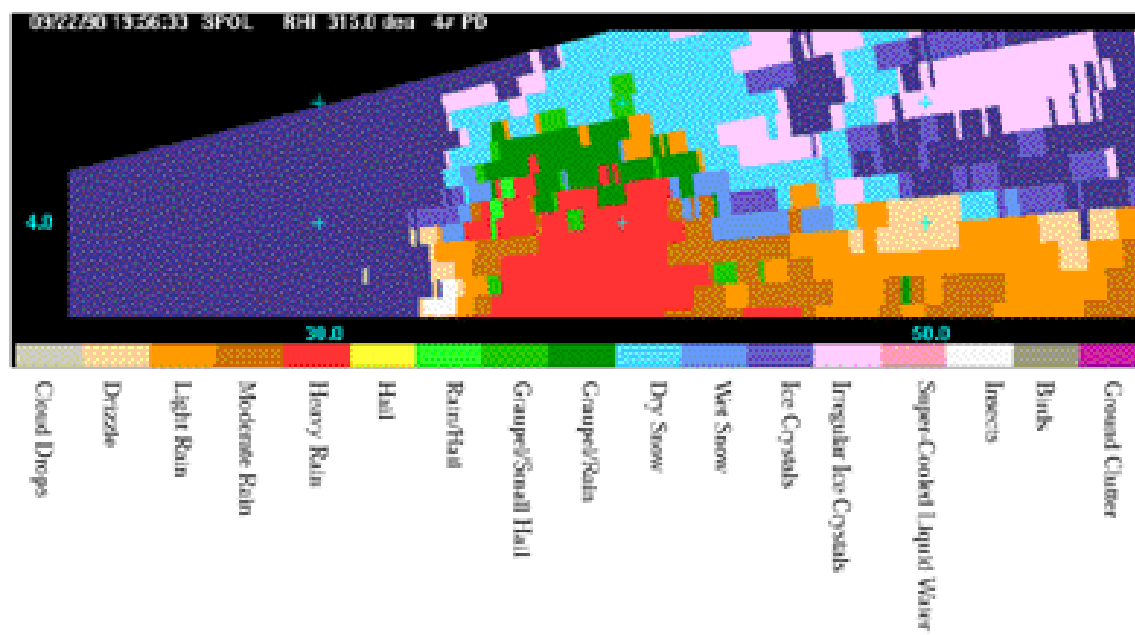


Fig. 4: Hydrometeor classifications for the storm in Fig. 3.

# Bayesian neural networks for MDA and TDA

Caren Marzban

## Abstract

In this report the development of two Bayesian neural networks for tornado diagnosis is outlined. The term Bayesian refers to the fact that the parameters of the network are drawn from distributions.

## 1 Method

The Neural Network (NN) work outlined here parallels that described in MOU99. The only major exception is in principal components analysis: The NN outlined in MOU99 was based on the principal components of the data. For the current (and much larger - 83 storm days) data set <sup>1</sup>, although many of the attributes are linearly correlated (over 90% of the variance in the data is explained by as few as 40 principal components), it was found that the NN does not benefit from this transformation, and so, the principal components were not employed.

Two NNs are developed, one for MDA detections and another for TDA detections. Each NN produces a probability of tornado (POT), conditioned on the respective attributes. The attributes (variables) are defined and numerically labeled in Appendix A. Henceforth, each of these variables will be referred to by the corresponding number.

The attributes include Near Storm Environment (NSE) variables (labeled with “d2d” in Appendix A. A comparison of the NNs that have NSE inputs (labeled as NN+NSE) with the NNs that do not (labeled as NN–NSE) is also performed.

Pairs of attributes for which the correlation coefficients for tornadic (1) and nontornadic (0) circulations are larger than 0.87 are given in Appendix B. It can be seen that many attributes are not independent and may be considered statistically equivalent.

---

<sup>1</sup>The data were produced by Gregory Stumpf, DeWayne Mitchell, and V. Lakshmanan of the National Severe Storms Laboratory.

Table 1: Sample sizes for nontornadic  $N_0$  and tornadic  $N_1$  circulations, and the prior (climatological) probability of tornado ( $p_1 = N_1/(N_0 + N_1)$ ) for circulations whose base extends as low as the  $n^{th}$  elevation angle.

	MDA			TDA		
$n$	$N_0$	$N_1$	$p_1$	$N_0$	$N_1$	$p_1$
1	24781	2198	0.081	5962	1408	0.191
2	9609	181	0.018	4091	205	0.047
3	6000	75	0.012	3606	68	0.018
4,5	4871	55	0.011	3128	48	0.015
6-10	3571	29	0.008	1968	38	0.018
11-13	268	0	0.000	187	3	0.015

## 2 Preprocessing

In a preliminary examination of the data it was found that a simple rule can correctly classify a large number of the circulations. Specifically, all rank=0 circulations in MDA are correctly classified as nontornadic. Also, for both MDA and TDA, almost all circulations whose base does not extend down as low as the third elevation angle (2.4 degrees) are correctly classified as nontornadic. As such, only the rank  $\neq 0$  circulations whose base extends down as low as one of the first three elevation angles (0.5, 1.5, 2.4 degrees) are retained for the NN development. The prior (climatological) probability of tornado (excluding rank=0 circulations) for a few elevation angles is given in Table 1.

The basic statistics of all the variables are computed. These include the mean, standard deviation, minimum, and maximum. These quantities aid in the first-round of error-discovery.

The missing values are replaced by the mean of the corresponding variable. The rare occurrence of the missing data obviates the need for more sophisticated techniques for handling missing data.

All the variables are centered via z-scores. This linear transformation renders the mean and the standard deviation of all the variables zero and one, respectively. In this way, it is possible to identify the outliers in the data, e.g., those due to de-aliasing. Specifically, all values with a z-score of 5, or larger, are filtered away.

Next, the collinearity of the attributes (Appendix B) is employed to eliminate some of the inputs. Only variables that have a linear correlation coefficient less than or equal to 0.87 with all other variables are retained for the analysis. This reduces the number of inputs from 177 and 144, for MDA and TDA, respectively, to 133, and 98.

The error function minimized in the training phase of the NN is cross-entropy. It is a consequence of this choice (and the choice of the logistic activation function, and the particular coding of ground truth in the output nodes), that allows the single output node to represent the (posterior) probability of tornado (POT), given the value of the attributes.

To reduce these probabilities to dichotomous variables for the purpose of computing categorical performance measures, a decision threshold is introduced. The threshold marks the boundary between forecasts of events and nonevents. It is varied from 0 to 1 in steps of 0.001, and at each point the value of some scalar measures is calculated. In this way, one can find both the maximum value of the measure and the probability threshold at which that value is obtained. Additionally, the performance of the NNs is assessed in terms of non-categorical (and probabilistic) measures.

### 3 Results

The number of hidden nodes is arrived at via bootstrapping. The optimal number of hidden nodes is found to be 8 for MDA and, and 4 for TDA. As such both NNs are highly nonlinear.

Several measures of performance have been utilized. The measures include Heidke's Skill Statistic (HSS), Probability of Detection(POD), and False Alarm Rate (FAR), Relative Operating Characteristic (ROC) curves, distributions of the probabilities, and their reliabilities. The definitions of all of these quantities are given in MOU99. Recall that an ROC curve is a parametric curve of POD versus False Alarm Ratio, as a threshold on POT varies from 0 to 1. A random classifier would have the diagonal line as its ROC curve, while a perfect classifier would have an ROC curve that traces the y- and the x-axis. Equivalently, the area under the ROC curve for a random classifier is 0.5, and that of a perfect classifier is 1.0.

The distributions of the POTs for tornadic (1) and nontornadic (0) circulations are given in Figure 1. Evidently, the NNs are capable of discriminating between the two classes.

Since the outputs of the NN have been designed to be posterior probabilities, then it is natural to examine their reliabilities. The reliability diagrams in Figure 2 show that the POTs are completely reliable within the statistical error bounds.

Figures 3 show the values of POD, FAR, and HSS as a function of the decision (probability) threshold placed on POT. The maximum obtained HSS values can be read from these graphs, and they are tabulated in Table 2. Note that the MDA NN outperforms the TDA NN at the critical value of the threshold.

As mentioned previously, ROC curves offer a two-dimensional representation of



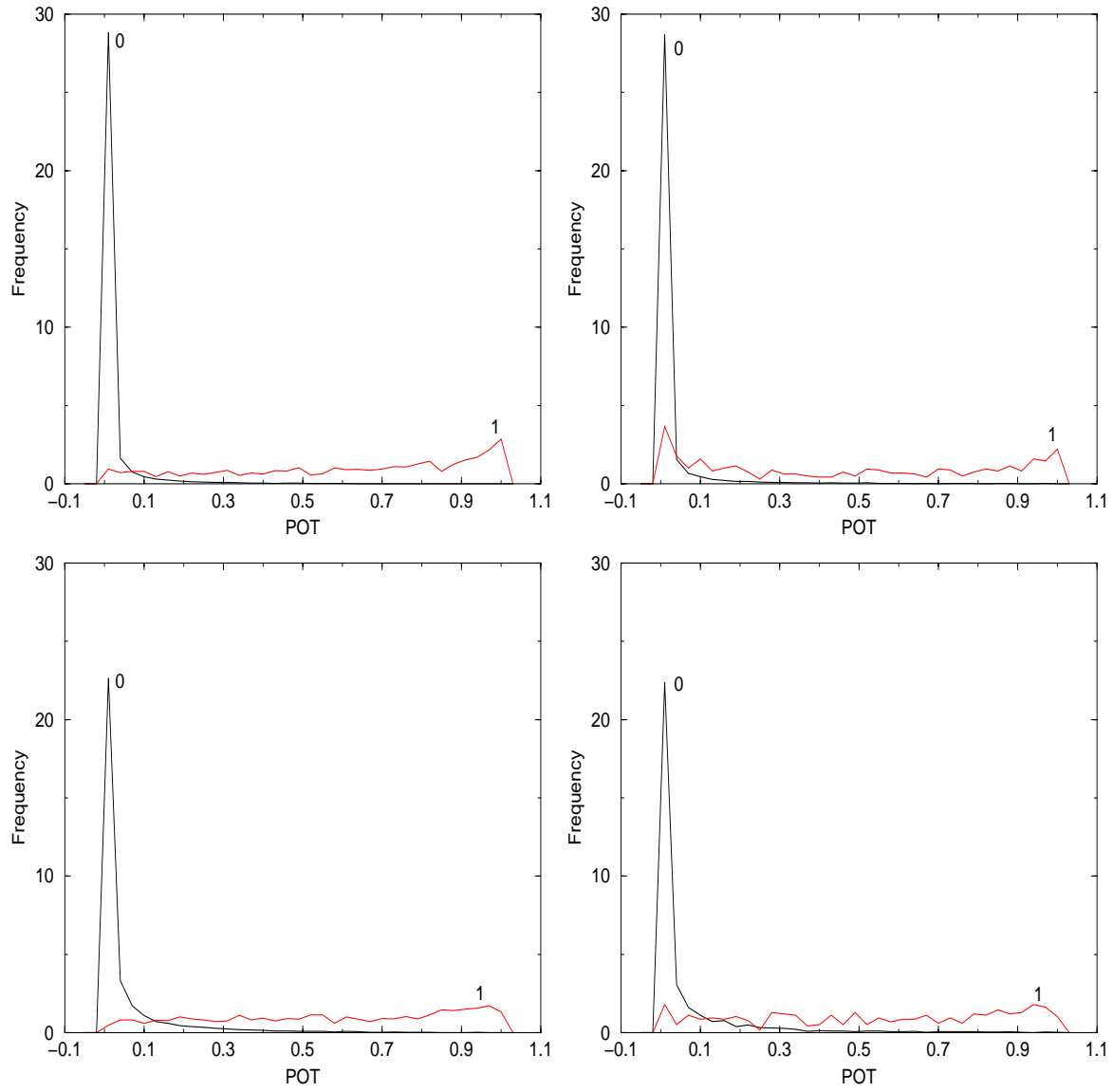


Figure 1: The distribution of POT for tornadic (1) and nontornadic (0) circulations for MDA NN (top), and TDA NN (bottom), for the training (left) and validation (right) set. The clear separation of the distribution of the 0s and the 1s reflects a high level of discriminatory power.

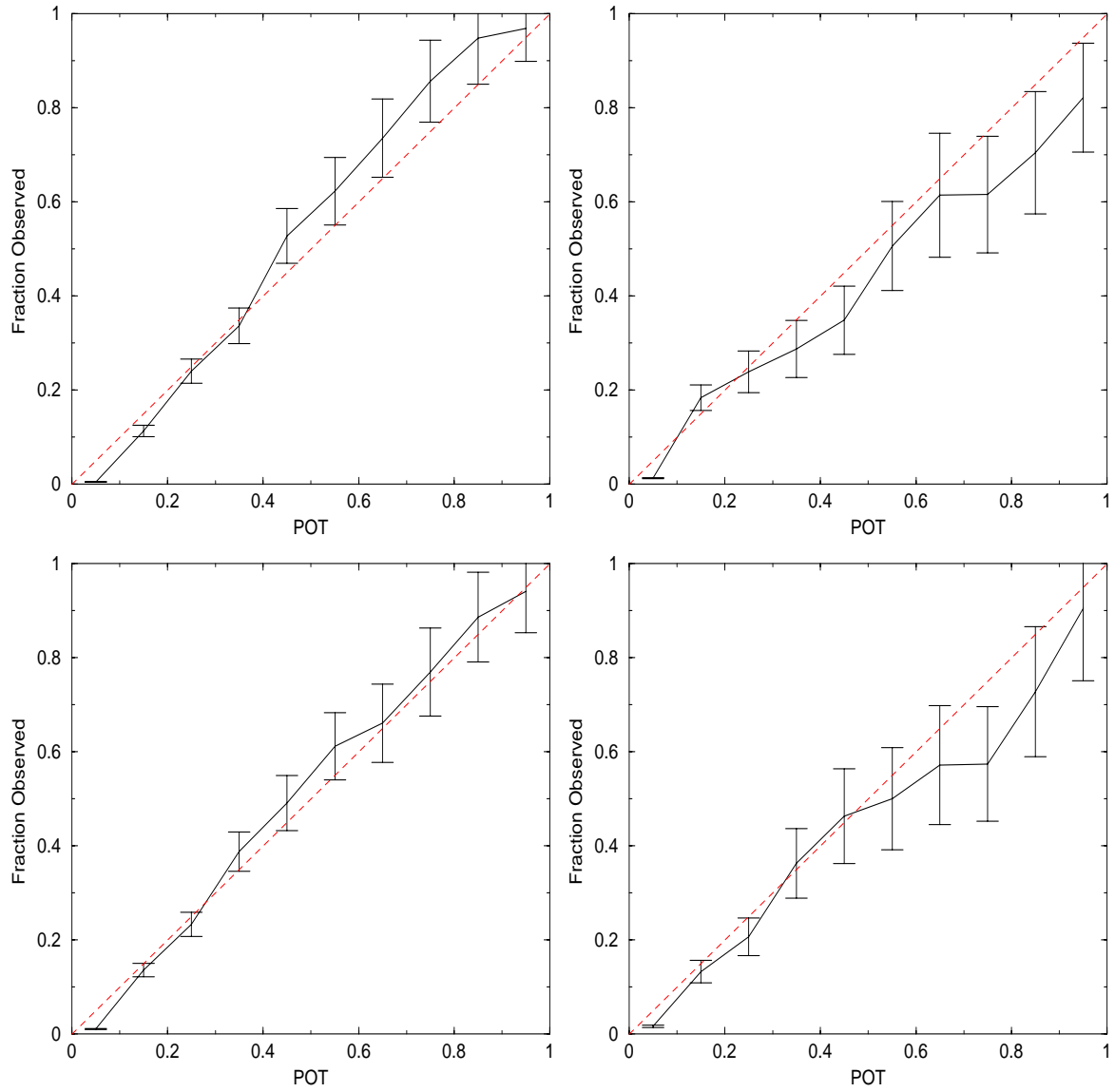


Figure 2: The reliability diagrams of the MDA NN (top), and TDA NN (bottom), for the training (left) and validation (right) set. The NNs have perfect reliability within the error bars.

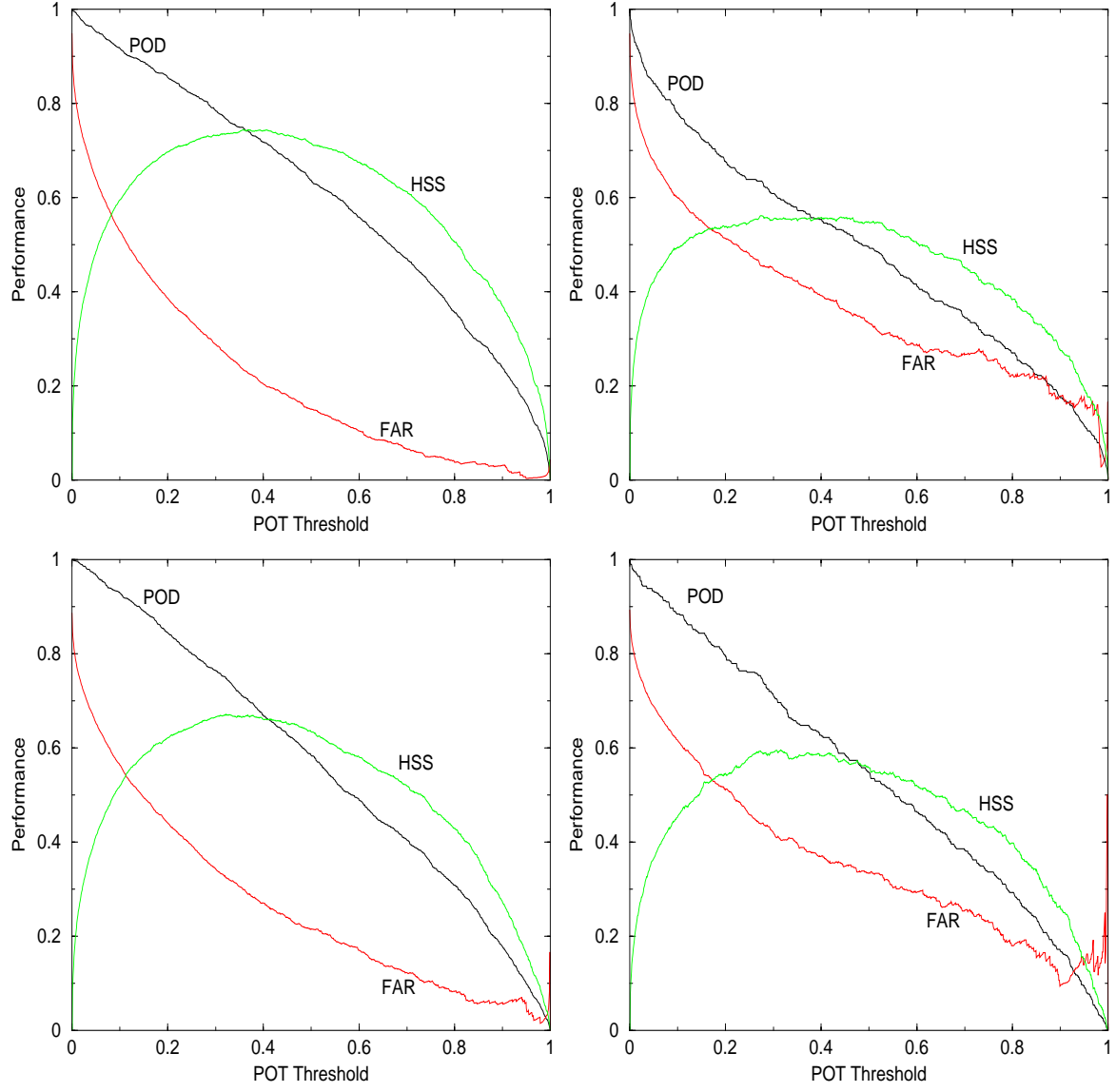


Figure 3: The performance of the MDA NN (top), and TDA NN (bottom), on the training (left) and validation (right) set, as a function of a threshold placed on POT.

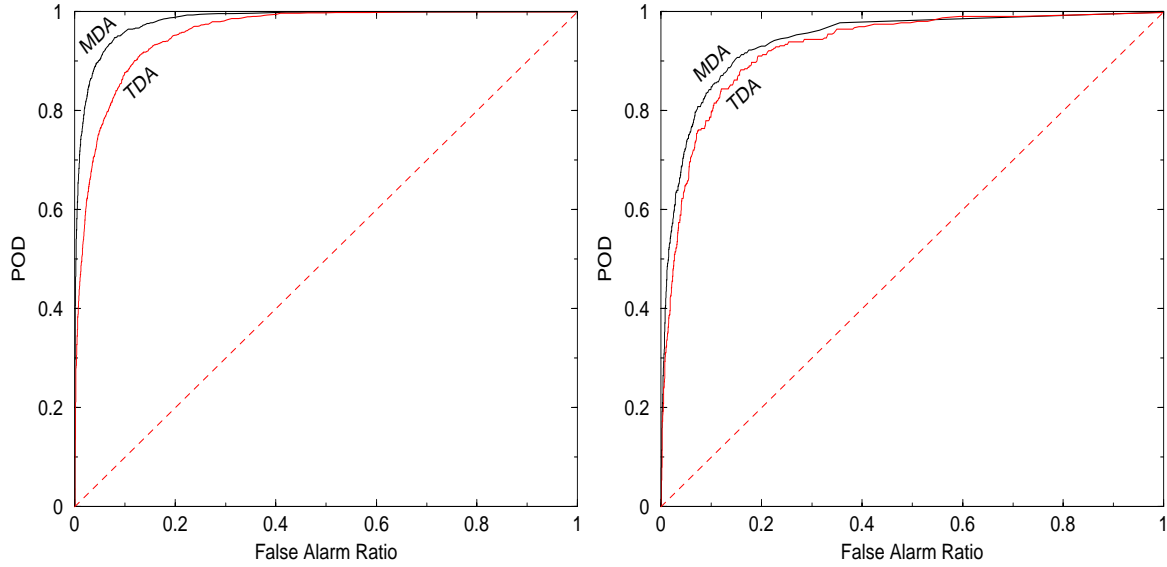


Figure 4: The ROC plots of the MDA and TDA NNs for the training (left) and validation (right) set.

Table 2: The HSS and ROC areas of the NNs with NSE inputs (NN+NSE) and the NNs without NSE inputs (NN−NSE).

		Training		Validation	
		HSS	ROC	HSS	ROC
NN+NSE	MDA	$0.740 \pm 0.003$	$0.982 \pm 0.000$	$0.567 \pm 0.003$	$0.942 \pm 0.000$
	TDA	$0.661 \pm 0.004$	$0.955 \pm 0.001$	$0.587 \pm 0.013$	$0.922 \pm 0.002$
NN−NSE	MDA	0.431	0.902	0.367	0.871
	TDA	0.434	0.855	0.407	0.844

performance that does not explicitly refer to a probability threshold, and so, is more user-independent than the other scalar measures. The ROC curves for the NNs are given in Figure 4. It can be seen that all of the NNs perform quite well. In particular, it is interesting that the MDA NN has higher performance than the TDA NN for all values of the threshold.

Finally, a comparison of the NNs that have NSE variable (labeled as NN+NSE) with the NNs that do not (labeled as NN−NSE) is given in Table 2. For this purpose, performance will be measured in terms of HSS and the area under the ROC curves. An area of 1 represents a perfect classifier, and an area of 0.5 reflects a random classifier. Although the error-bars for NN−NSE have not been computed, it is evident that the inclusion of NSE variables dramatically improves performance.

According the performance measures in Table 2, the current NNs perform compa-

Table 3: The performance of the NNs in terms of POD, FAR, and HSS for (NN $\pm$ NSE).

		Training			Validation		
		POD	FAR	HSS	POD	FAR	HSS
NN+	MDA	74	23	74	53	36	57
NSE	TDA	75	32	66	69	31	59
NN−	MDA	42	56	40	41	59	37
NSE	TDA	46	48	43	56	59	40

rably to the ones developed on a smaller data set in the past. This, in fact, suggests an improvement in the overall performance of the NNs because of the wider diversity present in the current data set. In other words, the fact that the current NNs can yield a performance similar to the older NNs, in spite of the larger data set, implies that the current NNs have better generalization capability and will therefore perform better in the field. The ultimate proof, however, will come when the two (older and newer) NNs can be tested on an independent data set. This data set is currently under construction.

## 4 Summary

Bayesian neural networks have been developed for the diagnosis of tornados. The performance of the NNs is gauged in terms of both probabilistic and categorical measures. It is shown that the NNs offer a high degree of discrimination, in addition to producing perfectly reliable probabilities. It is also found that the MDA NN generally outperforms the TDA NN.

For summary purposes, it is most convenient to report only the categorical performance measures, although such a practice does neglect the inherent two-dimensional nature of performance. These are given in Table 3.

As for the role of the NSE-related variables (i.e., those labeled by a “d2d” in Appendix A), it appears that the NNs with these variables do perform better than the NNs without them. The level of improvement depends on the measure of performance, and the algorithm (MDA or TDA).

## 5 Appendix A

This appendix lists the various attributes and their identifying numbers by which they are referenced in the text of the report.

### MDA

1 Meso Range (km) 2 Meso base (m) 3 Meso depth (m) 4 Meso strength rank  
5 Meso low-level diameter (m) 6 Meso maximum diameter (m) 7 Meso height of  
maximum diameter (m) 8 Meso low-level rotational velocity (m/s) 9 Meso maximum  
rotational velocity (m/s) 10 Meso height of maximum rotational velocity (m) 11  
Meso low-level shear (m/s/km) 12 Meso maximum shear (m/s/km) 13 Meso height  
of maximum shear (m) 14 Meso low-level gate-to-gate velocity difference (m/s) 15  
Meso maximum gate-to-gate velocity difference (m/s) 16 Meso height of maximum  
gate-to-gate velocity difference (m) 17 Meso core base (m) 18 Meso core depth (m) 19  
Meso age (min) 20 Meso strength index (MSI) wghtd by avg density 21 Meso strength  
index (MSIr) "rank" 22 Meso relative depth (%) 23 Meso low-level convergence (m/s)  
24 Meso mid-level convergence (m/s) 25 Meso Vertically-integrated rotational velocity  
(m/s) 26 Meso Vertically-integrated Shear (m/s/km) 27 Meso Vertically-integrated  
gate-to-gate vel. diff. (m/s) 28 Meso TREND base (m) 29 Meso TREND depth (m)  
30 Meso TREND strength rank 31 Meso TREND low-level diameter (m) 32 Meso  
TREND maximum diameter (m) 33 Meso TREND height of maximum diameter (m)  
34 Meso TREND low-level rotational velocity (m/s) 35 Meso TREND maximum  
rotational velocity (m/s) 36 Meso TREND height of maximum rotational velocity  
(m) 37 Meso TREND low-level shear (m/s/km) 38 Meso TREND maximum shear  
(m/s/km) 39 Meso TREND height of maximum shear (m) 40 Meso TREND low-  
level gate-to-gate velocity difference (m/s) 41 Meso TREND maximum gate-to-gate  
velocity difference (m/s) 42 Meso TREND height of maximum gate-to-gate velocity  
difference 43 Meso TREND strength index (MSI) wghtd by avg 44 Meso TREND  
strength index (MSIr) "rank" 45 Meso TREND relative depth (%) 46 Meso TREND  
low-level convergence (m/s) 47 Meso TREND mid-level convergence (m/s) 48 Meso  
TREND Vertically-integrated rotational velocity (m/s) 49 Meso TREND Vertically-  
integrated Shear (m/s/km) 50 Meso TREND Vertically-integrated gate-to-gate vel.  
diff. (m/s) 51 Meso Integrated Rotational Strength (IRS) index (NWS method 52  
Meso Integrated Rotational Strength (IRS) index (MSI method 53 BWER Overall  
Confidence (0-100%) 54 d2d actual surface pressure (mb) 55 d2d number of upper-  
air pressure levels lying below ground 56 d2d surface u-component (north-relative ;  
m/s) 57 d2d surface v-component (north-relative ; m/s) 58 d2d H253: height of the  
253 K temperature 59 d2d H273: height of the 273 K temperature 60 d2d UAVE:  
average u-component over a specified depth 61 d2d VAVE: average v-component over  
a specified depth 62 d2d average wind speed over a specified 63 d2d STSP: estimated  
storm speed (m/s) 64 d2d u-component of estimated storm motion vector(north-  
relative) 65 d2d v-component of estimated storm motion vector(north-relative) 66  
d2d same as 7, except for grid-relative 67 d2d same as 8, except for grid-relative 68

d2d same as 11, except for grid-relative 69 d2d same as 12, except for grid-relative 70  
 d2d SRH3: estimated 0-3 km storm relative helicity 71 d2d SFRH: surface relative  
 humidity (percent) 72 d2d AVRH: avg rel hum from surface to 73 d2d surface virtual  
 temperature (Kelvin) 74 d2d SCAP: Convective Available Pot Energy (CAPE) of 75  
 d2d SCIN: Convective Inhibition (CIN) of surface parcel 76 d2d SLFC: Level of Free  
 Convection (LFC) of 77 d2d SFEL: Equilibrium Level (EL) of surface parcel 78 d2d  
 SFLI: Lifted Index (LI) of surface parcel 79 d2d SEHI: Energy-Helicity Index (EHI) of  
 surface parcel 80 d2d SMPL: Maximum Parcel Level: level (m AGL) 81 d2d UCAP:  
 same as 21, except for the 82 d2d UCIN: same as 28, except for CIN 83 d2d ULFC:  
 same as 28, except for LFC 84 d2d UNEL: same as 28, except for EL 85 d2d UNLI:  
 same as 28, except for LI 86 d2d UEHI: same as 28, except for EHI 87 d2d UMPL:  
 same as 27, except for most unstable parcel in lowest 300 mb 88 d2d UHGT: height (m  
 AGL) of the most unstable (highest theta-e) parcel 89 d2d DDC1: downdraft CAPE  
 (dCAPE) for a parcel 1 km AGL 90 d2d DDC3: dCAPE for a parcel 3 km AGL 91  
 d2d DDC0: dCAPE for the parcel at 0 Celsius 92 d2d ACAP: same as 21, except  
 for a parcel with average characteristics 93 d2d ACIN: same as 39, except for CIN  
 94 d2d ALFC: same as 39, except for LFC 95 d2d AVEL: same as 39, except for EL  
 96 d2d AVLI: same as 39, except for LI 97 d2d AEHI: same as 39, except for EHI 98  
 d2d AMPL: same as 27, except for the "average" parcel 99 d2d SRLO: magnitude of  
 the storm-relative flow for the 0-2 km agl 100 d2d SRMD: same as 46, except for the  
 4-6 km agl layer 101 d2d SRHI: same as 46, except for the 9-11 km agl layer 102 d2d  
 SBRN: Bulk Richardson Number (BRN) calculated according 103 d2d BSHR: BRN  
 shear ( $kts^2$ ). See Eq. 3.4.58 104 d2d UBRN: same as 49, except for the most unstable  
 parcel. 105 d2d DT75: temperature difference (C) between 700 and 500 mb 106 d2d  
 LLSM: magnitude (kts) of the low-level shear 107 d2d VTOT: Vertical Totals Index  
 (C) 108 d2d CTOT: Cross Totals Index (C) 119 d2d TTOT: Total Totals Index (C)  
 110 d2d AM35: average wind speed in the 500-300 111 d2d MXTE: maximum theta-  
 e (Kelvin) in the lowest 300 mb 112 d2d MCNV: surface moisture convergence 113  
 d2d SSHR: wind speed at specified height minus surface wind speed 114 d2d AVOR:  
 mean absolute vorticity in a layer 115 d2d LAPS: mean lapse rate in the 850-500  
 116 d2d MSHR: mean shear through a specified depth 117 d2d WNDX: WINDEX  
 parameter (max gust potential in 118 d2d 06SM: 0-6 km shear magnitude (knots)  
 119 d2d DLSM: deep-layer shear vector magnitude (knots). 120 d2d SLCL: surface  
 parcel LCL (m agl).NOTE: convert 121 d2d ALCL: average parcel LCL (m agl). 122  
 d2d ULCL: most unstable parcel LCL (m agl). 123 d2d SARH: average RH (percent)  
 below the surface 124 d2d AARH: average RH (percent) below the average 125 d2d  
 UARH: average RH (percent) below the most unstable parcel's LCL 126 d2d SVGP:  
 Vorticity Generation Potential (VGP) using surface-based 127 d2d SCVT: convective  
 temperature (F) of surface parcel 128 d2d ACVT: same as 75, except for "average  
 parcel" 129 d2d PCPW: precipitable water in entire sounding 130 d2d DD70: dew  
 point depression at 700 mb 131 d2d DD50: dew point depression at 500 mb 132  
 d2d MXDD: maximum dew point depression in the 133 d2d HMTE: height (m agl)  
 of the minimum 134 d2d DDCU: dCAPE for the parcel defined in 135 d2d TEDF:  
 surface theta-e minus minimum theta-e below 136 d2d DDCL: dCAPE from the

surface parcel LCL 137 d2d OMEG: RUC-II vertical velocity (omega; microbars/sec)  
 138 d2d AOML: average omega (vertical velocity; microbars/sec) in the low 139 d2d  
 KIDX: K-Index (C) 140 d2d HLCY: RUC-II Helicity (m<sup>2</sup>/s<sup>2</sup>) 141 d2d CAPE: RUC-  
 II CAPE (J/kg) 142 d2d CINS: RUC-II CIN (J/kg) 143 d2d LIFT: RUC-II Lifted  
 Index (C) 144 d2d LFT4: RUC-II Another Lifted Index (C) 145 d2d USSI: Shear  
 Stability Index (SSI; W. Martin) 146 d2d SWIX: Showalter Index for MU parcel (K)  
 147 d2d SWET: Severe Weather (SWEAT) Index 148 d2d AMR1: Average Mixing  
 Ratio in 0-1 km layer 149 d2d AMR3: Average Mixing Ratio in 0-3 km layer 150  
 d2d AMR6: Average Mixing Ratio in 0-6 km layer 151 d2d SRH1: estimated 0-1  
 km storm relative helicity 152 d2d SRH2: estimated 0-2 km storm relative helicity  
 153 d2d ARH1: Average Relative Humidity in 0-1 km layer 154 d2d 01SM: 0-1 km  
 shear magnitude (knots) 155 d2d 03SM: 0-3 km shear magnitude (knots) 156 d2d  
 27SM: 27% UNEL (corresp. to 0-3 km) shear magnitude 157 d2d 55SM: 55% UNEL  
 (corresp. to 0-6 km) shear magnitude 158 d2d 18SR: 0-18% UNEL (corresp. to 0-2  
 km) storm-relative flow 159 d2d 55SR: 36-55% UNEL (corresp. to 4-6 km) storm-  
 relative flow 160 d2d 82SR: 82-100% UNEL (corresp. to 9-11 km) storm-relative flow  
 161 d2d ULMB: Level of Maximum Bouyancy (from most-unstable parcel) 162 d2d  
 UMXB: Maximum Bouyancy (from most-unstable parcel) 163 d2d MBSM: ULMB  
 (corresp. to 0-6 km) shear magnitude 164 d2d MBSR: 20% below ULMB (corresp.  
 to 4-6km) storm-relative flow 165 d2d HODO: 0-6km Bulk Hodograph Curvature  
 (=0 straight; 166 d2d LLLR: Low-Level (ULFC to ULFC+1km) Lapse Rate 167 d2d  
 SNCA: Normalized SCAP [divide by z(SFEL)-z(SLFC)] 168 d2d UNCA: Normalized  
 UCAP [divide by z(UNEL)-z(ULFC)] 169 d2d ANCA: Normalized ACAP [divide  
 by z(AVEL)-z(ALFC)] 170 d2d UCA3: UCAP from ULFC to ULFC+3km 171 d2d  
 UNC3: UCAP from ULFC to ULFC+3km divided by UCAP 172 d2d UCAB: UCAP  
 from sfc to 3 km 173 d2d UNCB: UCAP from sfc to 3 km AGL divided by UCAP 174  
 d2d SR20: Storm-relative flow (knots) at H253 level 175 d2d AMEL: Average wind  
 speed (kts) in 100 mb layer surrounding UNEL. 176 d2d AWB7: Average wet bulb  
 temp (K) from sfc to 700 mb. 177 d2d HWBZ: Height (m) of the level at which the  
 wet-bulb temp = 273K.

## TDA

1. TVS base (m) [0-8000] 2. TVS depth (m) [0-10000] 3. TVS low-level gate-to-  
 gate velocity difference (m/s) [0-90] 4. TVS maximum gate-to-gate velocity difference  
 (m/s) [0-90] 5. TVS height of maximum gate-to-gate velocity difference (m) [1-11000]  
 6. TVS low-level shear (m/s/km) [0-350] 7. TVS maximum shear (m/s/km) [0-350] 8.  
 TVS height of maximum shear (m) [1-11000] 9. TVS Tornado Strength Index (TSI)  
 10. TVS TREND base (m) [-8000-8000] 11. TVS TREND depth (m) [-10000-10000]  
 12. TVS TREND low-level gate-to-gate velocity difference (m/s) [-90-90] 13. TVS  
 TREND maximum gate-to-gate velocity difference (m/s) [-90-90] 14. TVS TREND ht  
 of max gate-to-gate velocity difference (m) [-11000-11000] 15. TVS TREND low-level  
 shear (m/s/km) [-350-350] 16. TVS TREND maximum shear (m/s/km) [-350-350] 17.



TVS TREND height of maximum shear (m) [-11000-11000] 18. TVS TREND Tornado Strength Index (TSI) 19. TVS Range (km) [0-150] 20. d2d actual surface pressure (mb) 21. d2d number of upper-air pressure levels lying below ground 22. d2d surface u-component (north-relative ; m/s) 23. d2d surface v-component (north-relative ; m/s) 24. d2d H253: height of the 253 K temperature surface (m agl) 25. d2d H273: height of the 273 K temperature surface (m agl) 26. d2d UAVE: average u-component over a specified depth 27. d2d VAVE: average v-component over a specified depth 28. d2d average wind speed over a specified depth (m/s) 29. d2d STSP: estimated storm speed (m/s) 30. d2d u-component of estimated storm motion vector 31. d2d v-component of estimated storm motion vector 32. d2d same as 7, except for grid-relative. 33. d2d same as 8, except for grid-relative 34. d2d same as 11, except for grid-relative 35. d2d same as 12, except for grid-relative 36. d2d SRH3: estimated 0-3 km storm relative helicity ( $m^2/s^2$ ) 37. d2d SFRH: surface relative humidity (percent) 38. d2d AVRH: average relative humidity from the surface to the height 39. d2d surface virtual temperature (Kelvin) 40. d2d SCAP: Convective Available Potential Energy (CAPE) of surface 41. d2d SCIN: Convective Inhibition (CIN) of surface parcel (J/kg) 42. d2d SLFC: Level of Free Convection (LFC) of surface parcel (m AGL) 43. d2d SFEL: Equilibrium Level (EL) of surface parcel (m AGL) 44. d2d SFLI: Lifted Index (LI) of surface parcel (degrees) 45. d2d SEHI: Energy-Helicity Index (EHI) of surface parcel 46. d2d SMPL: Maximum Parcel Level: level (m AGL) at which the negative 47. d2d UCAP: same as 21, except for the most unstable parcel 48. d2d UCIN: same as 28, except for CIN 49. d2d ULFC: same as 28, except for LFC 50. d2d UNEL: same as 28, except for EL 51. d2d UNLI: same as 28, except for LI 52. d2d UEHI: same as 28, except for EHI 53. d2d UMPL: same as 27, except for the most unstable parcel in lowest 54. d2d UHGT: height (m AGL) of the most unstable (highest theta-e) parcel 55. d2d DDC1: downdraft CAPE (dCAPE) for a parcel 1 km AGL 56. d2d DDC3: dCAPE for a parcel 3 km AGL 57. d2d DDC0: dCAPE for the parcel at 0 Celsius 58. d2d ACAP: same as 21, except for parcel with average characteristics 59. d2d ACIN: same as 39, except for CIN 60. d2d ALFC: same as 39, except for LFC 61. d2d AVEL: same as 39, except for EL 62. d2d AVLI: same as 39, except for LI 63. d2d AEHI: same as 39, except for EHI 64. d2d AMPL: same as 27, except for the "average" parcel 65. d2d SRLO: magnitude of the storm-relative flow for the 0-2 km agl 66. d2d SRMD: same as 46, except for the 4-6 km agl layer 67. d2d SRHI: same as 46, except for the 9-11 km agl layer 68. d2d SBRN: Bulk Richardson Number (BRN) calculated according to 69. d2d BSHR: BRN shear ( $kts^2$ ). See Eq. 3.4.58 of Bluestein Vol. II. 70. d2d UBRN: same as 49, except for the most unstable parcel. 71. d2d DT75: temperature difference (C) between 700 and 500 mb. 72. d2d LLSM: magnitude (kts) of the low-level shear vector 73. d2d VTOT: Vertical Totals Index (C) 74. d2d CTOT: Cross Totals Index (C) 75. d2d TTOT: Total Totals Index (C) 76. d2d AM35: average wind speed in the 500-300 mb layer (knots) 77. d2d MXTE: maximum theta-e (Kelvin) in the lowest 300 mb 78. d2d MCNV: surface moisture convergence [ (g/kg)/hr ] 79. d2d SSHR: (wind speed at specified height - surface wind speed) (kts) 80. d2d AVOR: mean absolute vorticity in a layer ( $\times 10^5 sec^{-1}$ ) 81. d2d LAPS: mean lapse rate in the 850-500 mb layer (C/km) 82.

d2d MSHR: mean shear through a specified depth 83. d2d this is a dummy element  
 84. d2d WNDX: WINDEX parameter (max gust potential in knots) 85. d2d 06SM:  
 0-6 km shear magnitude (knots) 86. d2d DSLM: deep-layer shear vector magnitude  
 (knots). 87. d2d SLCL: surface parcel LCL (m agl). 88. d2d ALCL: average parcel  
 LCL (m agl). See NOTE above. 89. d2d ULCL: most unstable parcel LCL (m agl).  
 See NOTE above. 90. d2d SARH: average RH (percent) below the surface parcel's  
 LCL 91. d2d AARH: average RH (percent) below the average parcel's LCL 92. d2d  
 UARH: average RH (percent) below the most unstable parcel's LCL 93. d2d SVGP:  
 Vorticity Generation Potential (VGP) using surface-based 94. d2d SCVT: convective  
 temperature (F) of surface parcel 95. d2d ACVT: same as 75, except for "average  
 parcel" 96. d2d PCPW: precipitable water in entire sounding (inches) 97. d2d DD70:  
 dew point depression at 700 mb (Kelvin) 98. d2d DD50: dew point depression at  
 500 mb (Kelvin) 99. d2d MXDD: max dew point depression in the layer 700-400  
 mb (Kelvin) 100. d2d HMTE: height (m agl) of the minimum theta-e below 400  
 mb 101. d2d DDCU: dCAPE for the parcel defined in d2d(81, 102. d2d TEDF:  
 surface theta-e minus minimum theta-e below 400 mb (K) 103. d2d DDCL: dCAPE  
 from the surface parcel LCL in d2d(68, 104. d2d OMEG: vertical velocity (omega;  
 microbars/sec) at a specified 105. d2d AOML: average omega (vertical velocity;  
 microbars/sec) in the 106. d2d KIDX:: K-Index (C) 107. d2d HLCY:: RUC-II  
 Helicity ( $m^2/s^2$ ) 108. d2d CAPE:: RUC-II CAPE (J/kg) 109. d2d CINS:: RUC-II  
 CIN (J/kg) 110. d2d LIFT:: RUC-II Lifted Index (C) 111. d2d LFT4:: RUC-II  
 Another Lifted Index (C) 112. d2d USSI: Shear Stability Index (SSI; W. Martin) for  
 MU parcel 113. d2d SWIX:: Showalter Index for MU parcel (K) 114. d2d SWET::  
 Severe Weather (SWEAT) Index 115. d2d AMR1: Average Mixing Ratio in 0-1 km  
 layer (g/kg) 116. d2d AMR3: Average Mixing Ratio in 0-3 km layer (g/kg) 117. d2d  
 AMR6: Average Mixing Ratio in 0-6 km layer (g/kg) 118. d2d SRH1: estimated  
 0-1 km storm relative helicity ( $m^2/s^2$ ) 119. d2d SRH2: estimated 0-2 km storm  
 relative helicity ( $m^2/s^2$ ) 120. d2d ARH1: Average Relative Humidity in 0-1 km layer  
 (%) 121. d2d 01SM: 0-1 km shear magnitude (knots) 122. d2d 03SM: 0-3 km shear  
 magnitude (knots) 123. d2d 27SM: 27% UNEL (corresp. to 0-3 km) shear magnitude  
 (knots) 124. d2d 55SM: 55% UNEL (corresp. to 0-6 km) shear magnitude (knots)  
 125. d2d 18SR: 0-18% UNEL (corresp. to 0-2 km) storm-relative flow (knots) 126.  
 d2d 55SR: 36-55% UNEL (corresp. to 4-6 km) storm-relative (knots) 127. d2d 82SR:  
 82-100% UNEL (corresp. to 9-11 km) storm-relative (knots) 128. d2d ULMB: Level  
 of Maximum Bouyancy (most-unstable parcel) (m AGL) 129. d2d UMXB: Maximum  
 Bouyancy (from most-unstable parcel) ( $m^2/s^2$ ) 130. d2d MBSM: ULMB (corresp.  
 to 0-6 km) shear magnitude (knots) 131. d2d MBSR: 20% below ULMB (corresp.  
 to 4-6 km) storm-relative flow 132. d2d HODO: 0-6km Bulk Hodograph Curvature  
 133. d2d LLLR: Low-Level (ULFC to ULFC+1km) Lapse Rate (C/km) 134. d2d  
 SNCA: Normalized SCAP [divide by  $z(SFEL)-z(SLFC)$ ] 135. d2d UNCA: Normalized  
 UCAP [divide by  $z(UNEL)-z(ULFC)$ ] 136. d2d ANCA: Normalized ACAP [divide by  
 $z(AVEL)-z(ALFC)$ ] 137. d2d UCA3: UCAP from ULFC to ULFC+3km 138. d2d  
 UNC3: UCAP from ULFC to ULFC+3km divided by UCAP (%age of total) 139.  
 d2d UCAB: UCAP from sfc to 3 km AGL 140. d2d UNCB: UCAP from sfc to 3 km

AGL divided by UCAP (%age of total) 141. d2d SR20: Storm-relative flow (knots) at H253 (1km surrounding). 142. d2d AMEL: Average wind speed (kts) in 100 mb layer surrounding UNEL. 143. d2d AWB7: Average wet bulb temp (K) from sfc to 700 mb. 144. d2d HWBZ: Height (m) of the level at which the wet-bulb temp = 273K.

## 6 Appendix B

This appendix lists the pair of variables that have a linear correlation coefficient larger than or equal to 0.87 for both nontornadic and tornadic circulations. Such pair of variables may be considered statistically equivalent.

MDA:

(21,20): $r_0=0.878$ , $r_1=0.920$	(128,127): $r_0=0.943$ , $r_1=0.945$
(25,9): $r_0=0.887$ , $r_1=0.885$	(136,120): $r_0=0.900$ , $r_1=0.882$
(25,20): $r_0=0.890$ , $r_1=0.930$	(138,137): $r_0=-0.999$ , $r_1=-1.000$
(26,12): $r_0=0.889$ , $r_1=0.886$	(140,137): $r_0=1.000$ , $r_1=1.000$
(27,15): $r_0=0.889$ , $r_1=0.894$	(140,138): $r_0=-0.999$ , $r_1=-0.999$
(40,34): $r_0=0.895$ , $r_1=0.872$	(141,137): $r_0=0.986$ , $r_1=0.988$
(48,35): $r_0=0.930$ , $r_1=0.886$	(141,138): $r_0=-0.986$ , $r_1=-0.988$
(48,43): $r_0=0.914$ , $r_1=0.927$	(141,140): $r_0=0.987$ , $r_1=0.988$
(50,41): $r_0=0.920$ , $r_1=0.875$	(142,137): $r_0=1.000$ , $r_1=1.000$
(50,43): $r_0=0.896$ , $r_1=0.897$	(142,138): $r_0=-0.999$ , $r_1=-1.000$
(50,48): $r_0=0.916$ , $r_1=0.890$	(142,140): $r_0=1.000$ , $r_1=1.000$
(52,9): $r_0=0.881$ , $r_1=0.877$	(142,141): $r_0=0.986$ , $r_1=0.988$
(52,20): $r_0=0.902$ , $r_1=0.934$	(143,137): $r_0=1.000$ , $r_1=1.000$
(52,21): $r_0=0.906$ , $r_1=0.939$	(143,138): $r_0=-0.999$ , $r_1=-1.000$
(52,25): $r_0=0.958$ , $r_1=0.967$	(143,140): $r_0=1.000$ , $r_1=1.000$
(52,27): $r_0=0.892$ , $r_1=0.909$	(143,141): $r_0=0.986$ , $r_1=0.988$
(55,54): $r_0=-0.963$ , $r_1=-0.965$	(143,142): $r_0=1.000$ , $r_1=1.000$
(59,58): $r_0=0.895$ , $r_1=0.897$	(144,137): $r_0=1.000$ , $r_1=1.000$
(63,62): $r_0=0.998$ , $r_1=0.997$	(144,138): $r_0=-0.999$ , $r_1=-1.000$
(64,60): $r_0=0.961$ , $r_1=0.890$	(144,140): $r_0=1.000$ , $r_1=1.000$
(65,61): $r_0=0.898$ , $r_1=0.976$	(144,141): $r_0=0.986$ , $r_1=0.988$
(66,60): $r_0=0.966$ , $r_1=0.952$	(144,142): $r_0=1.000$ , $r_1=1.000$
(67,61): $r_0=0.902$ , $r_1=0.975$	(144,143): $r_0=1.000$ , $r_1=1.000$
(68,60): $r_0=0.967$ , $r_1=0.911$	(149,148): $r_0=0.901$ , $r_1=0.895$
(68,64): $r_0=0.983$ , $r_1=0.953$	(150,149): $r_0=0.974$ , $r_1=0.971$
(68,66): $r_0=0.954$ , $r_1=0.924$	(151,70): $r_0=0.997$ , $r_1=0.941$
(69,61): $r_0=0.946$ , $r_1=0.964$	(153,121): $r_0=-0.966$ , $r_1=-0.982$
(69,67): $r_0=0.921$ , $r_1=0.964$	(153,123): $r_0=0.955$ , $r_1=0.953$
(80,77): $r_0=0.992$ , $r_1=0.988$	(153,124): $r_0=0.985$ , $r_1=0.982$
(92,81): $r_0=0.898$ , $r_1=0.937$	(154,106): $r_0=1.000$ , $r_1=1.000$
(97,86): $r_0=0.895$ , $r_1=0.958$	(156,106): $r_0=0.964$ , $r_1=0.961$
(98,95): $r_0=0.948$ , $r_1=0.971$	(156,154): $r_0=0.964$ , $r_1=0.961$
(120,71): $r_0=-0.973$ , $r_1=-0.984$	(157,155): $r_0=0.912$ , $r_1=0.934$
(123,71): $r_0=0.899$ , $r_1=0.884$	(162,81): $r_0=0.954$ , $r_1=0.960$
(123,121): $r_0=-0.932$ , $r_1=-0.948$	(162,92): $r_0=0.881$ , $r_1=0.923$
(124,121): $r_0=-0.957$ , $r_1=-0.971$	(177,176): $r_0=0.937$ , $r_1=0.935$
(124,123): $r_0=0.970$ , $r_1=0.975$	

TDA:

(7,6):  $r_0=0.897, r_1=0.905$   
(8,5):  $r_0=0.967, r_1=0.957$   
(9,7):  $r_0=0.885, r_1=0.876$   
(17,14):  $r_0=0.976, r_1=0.951$   
(22,21):  $r_0=-0.966, r_1=-0.969$   
(26,25):  $r_0=0.878, r_1=0.887$   
(30,29):  $r_0=0.998, r_1=0.997$   
(32,28):  $r_0=0.952, r_1=0.982$   
(33,27):  $r_0=0.973, r_1=0.947$   
(34,28):  $r_0=0.969, r_1=0.974$   
(34,32):  $r_0=0.877, r_1=0.936$   
(35,27):  $r_0=0.946, r_1=0.896$   
(35,31):  $r_0=0.977, r_1=0.949$   
(35,33):  $r_0=0.942, r_1=0.911$   
(36,28):  $r_0=0.957, r_1=0.965$   
(36,32):  $r_0=0.969, r_1=0.969$   
(36,34):  $r_0=0.939, r_1=0.973$   
(47,44):  $r_0=0.991, r_1=0.988$   
(58,57):  $r_0=0.933, r_1=0.921$   
(59,48):  $r_0=0.892, r_1=0.931$   
(63,52):  $r_0=0.879, r_1=0.929$   
(63,59):  $r_0=-0.878, r_1=-0.897$   
(64,53):  $r_0=0.906, r_1=0.962$   
(65,62):  $r_0=0.954, r_1=0.967$   
(82,74):  $r_0=-0.981, r_1=-0.985$   
(86,68):  $r_0=0.949, r_1=0.940$   
(87,38):  $r_0=-0.976, r_1=-0.982$   
(88,56):  $r_0=0.917, r_1=0.891$   
(90,38):  $r_0=0.903, r_1=0.872$   
(90,88):  $r_0=-0.947, r_1=-0.952$   
(91,56):  $r_0=-0.936, r_1=-0.901$   
(91,88):  $r_0=-0.963, r_1=-0.976$   
(91,90):  $r_0=0.975, r_1=0.977$   
(95,94):  $r_0=0.952, r_1=0.942$   
(99,98):  $r_0=0.873, r_1=0.870$   
(102,41):  $r_0=0.902, r_1=0.895$   
(103,87):  $r_0=0.925, r_1=0.887$   
(105,104):  $r_0=-1.000, r_1=-1.000$

(107,104):  $r_0=1.000, r_1=1.000$   
(107,105):  $r_0=-0.999, r_1=-0.999$   
(108,104):  $r_0=0.989, r_1=0.989$   
(108,105):  $r_0=-0.988, r_1=-0.988$   
(108,107):  $r_0=0.989, r_1=0.989$   
(109,104):  $r_0=1.000, r_1=1.000$   
(109,105):  $r_0=-1.000, r_1=-1.000$   
(109,107):  $r_0=1.000, r_1=1.000$   
(109,108):  $r_0=0.989, r_1=0.989$   
(110,104):  $r_0=1.000, r_1=1.000$   
(110,105):  $r_0=-1.000, r_1=-1.000$   
(110,107):  $r_0=1.000, r_1=1.000$   
(110,108):  $r_0=0.989, r_1=0.989$   
(110,109):  $r_0=1.000, r_1=1.000$   
(111,104):  $r_0=1.000, r_1=1.000$   
(111,105):  $r_0=-1.000, r_1=-1.000$   
(111,107):  $r_0=1.000, r_1=1.000$   
(111,108):  $r_0=0.989, r_1=0.989$   
(111,109):  $r_0=1.000, r_1=1.000$   
(111,110):  $r_0=1.000, r_1=1.000$   
(113,76):  $r_0=-0.878, r_1=-0.882$   
(116,96):  $r_0=0.941, r_1=0.936$   
(116,115):  $r_0=0.881, r_1=0.891$   
(117,96):  $r_0=0.987, r_1=0.986$   
(117,116):  $r_0=0.966, r_1=0.966$   
(118,37):  $r_0=0.955, r_1=0.937$   
(120,56):  $r_0=-0.938, r_1=-0.912$   
(120,88):  $r_0=-0.972, r_1=-0.986$   
(120,90):  $r_0=0.962, r_1=0.955$   
(120,91):  $r_0=0.986, r_1=0.984$   
(121,73):  $r_0=1.000, r_1=1.000$   
(123,73):  $r_0=0.968, r_1=0.963$   
(123,121):  $r_0=0.968, r_1=0.963$   
(124,122):  $r_0=0.931, r_1=0.949$   
(129,48):  $r_0=0.953, r_1=0.955$   
(129,52):  $r_0=-0.882, r_1=-0.890$   
(129,59):  $r_0=0.872, r_1=0.917$   
(144,143):  $r_0=0.949, r_1=0.940$

Jian Zhang<sup>1</sup>, Jonathan J. Gourley<sup>1</sup>, Ken Howard<sup>2</sup>, Bob Maddox<sup>1</sup><sup>1</sup>Cooperative Institute for Mesoscale Meteorological Studies, Norman, OK<sup>2</sup>NOAA/National Severe Storms Laboratory, Norman, OK

## 1. INTRODUCTION

The deployment of the United States NEXRAD (NWS's NEXt generation RADar, the NEXRAD or WSR-88D) network has provided weather forecasters an important tool in the monitoring of severe weather and for issuance of storm warnings. The current operational radar algorithms are based on single radar and are applied in polar coordinates. However, most forecast offices and regional aviation control centers monitor weather and storms over a geographical domain that encompasses several radar umbrellas. Further, the life cycle of an individual storm may be sampled by two or more radars requiring additional radars for better monitoring of storm characteristics and evolution.

The creation of a 3D radar mosaic would allow users and algorithm developers the benefit to use and develop a wide variety of products and displays that more fully depicts the evolution and lifecycle of storms. Examples include more physically realistic horizontal or vertical cross-sections. Single radar algorithms could be expanded to utilize data from multiple radars and other environmental data to more accurately determine storm attributes. Gridded radar data can also be easily combined with information from other data sources such as satellite data, model analyses or forecast fields increasing its value in the overall forecast and warning process. Regional rainfall maps using multisensor approaches are examples of such an application.

Gridding radar data is challenging due to 1) the conical geometry of radar sampling and 2) the large volume of radar data sets. The distribution of radar data is non-uniform in space, with high resolution in the radial direction and low resolution in azimuthal and elevational directions, especially at far ranges.

Corresponding author address: Jian Zhang, NSSL, 1313 Halley Circle, Norman, OK 73069.  
Email: jzhang@nssl.noaa.gov

Figure 1.1 shows radar data distributions on a x-z plane in Volume Coverage Pattern (VCP) 21. Near radar, the centers of data bins are spaced by about 1 km, while at far range they are spaced as much as 100 km horizontally and 5 km vertically. This non-uniformity makes the choice of an interpolation scheme and associated filter nontrivial. Trapp and Doswell (2000) tested nearest neighbor, a Barnes-type, and Cressman-type interpolation schemes. Their results show that a nearest neighbor scheme gives the smallest root-mean-square (RMS) errors, but the spatial scales of error fields are non-uniform. A strong Barnes filter based on

the poorest resolution in a reflectivity field results in a uniformly scaled error field, but significant high-resolution information in the observations is lost. This is not a desirable feature for monitoring severe storms by observation or by the use of an algorithmic procedure.

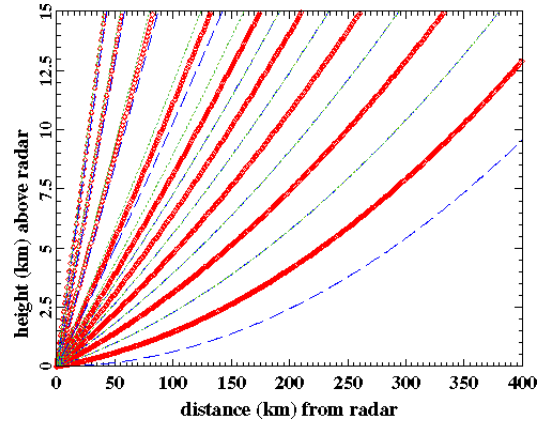


Fig. 1.1 Radar data distributions on a x-z plane in VCP 21. The circles represent the centers of radar bins; the dashed lines indicate the bottom of radar beams, and the dotted lines the top of radar beams. Note that the circles are overlapped on the top of each other at the lower elevation angles.

In this study, we choose an adaptive Barnes-type scheme (Askelson et al., 2000) for interpolating radar data onto a Cartesian grid. This scheme is designed for retaining high-resolution information in the original radar observations while filtering small-scale noise. In comparison to a uniform Barnes scheme, the adaptive Barnes scheme results in smaller errors in the interpolated fields, especially in regions near radar. Errors in analyzed reflectivity fields must be minimized when producing scalar fields such as precipitation rates and vertically integrated liquid (VIL).

## 2. CONICAL TO CARTESIAN TRANSFORMATION

The weighting function of the adaptive Barnes filter is defined as:

$$w_{i,k} = \exp \left[ -\frac{(r_k - r_i)^2}{\kappa_r} - \frac{(\phi_k - \phi_i)^2}{\kappa_\phi} - \frac{(\theta_k - \theta_i)^2}{\kappa_\theta} \right] \quad (2.1)$$

where,  $r_i$ ,  $\phi_i$ ,  $\theta_i$  are range, azimuth, and elevation of the  $i^{\text{th}}$  grid point;  $r_k$ ,  $\phi_k$ ,  $\theta_k$  are range, azimuth, and elevation of the center of  $k^{\text{th}}$  reflectivity observation bin in the influence region\* of the  $i^{\text{th}}$  grid point;  $\kappa_r$ ,  $\kappa_\phi$ ,  $\kappa_\theta$  are Barnes smoothing factors in the radial ( $r$ -), azimuthal ( $\phi$ -), and elevational ( $\theta$ -) directions, and  $w_{i,k}$  is weight given to the  $k^{\text{th}}$  reflectivity observation at the  $i^{\text{th}}$  grid point.

The interpolated value at the  $i^{\text{th}}$  grid point is calculated by:

$$f_i^a = \frac{\sum_{k=1}^{\text{nobs}} w_{i,k} f_k^o}{\sum_{k=1}^{\text{nobs}} w_{i,k}} \quad (2.2)$$

Here,  $f_i^a$  represents the interpolated reflectivity at the  $i^{\text{th}}$  grid point,  $f_k^o$  is the observed reflectivity at the  $k^{\text{th}}$  radar bin, and “nobs” represents the number of radar bins within the influence region of the  $i^{\text{th}}$  grid point.

In the adaptive Barnes scheme, there is approximately the same number of data points within the influence region of each grid point. The algorithm is computationally efficient since the number of data points is small when the filter is designed to retain high-resolution information in the raw data. On the other hand, a uniform Barnes scheme with large smoothing factors is computationally expensive because the number of data points within an influence region becomes very large at close ranges (Fig.1.1).

\* The influence region is a volume that is centered at a grid point and bounded by constant radial, azimuth and elevation distances ( $R_{i,r}$ ,  $R_{i,\phi}$ , and  $R_{i,\theta}$ ) away from the grid point.  $R_{i,r}$ ,  $R_{i,\phi}$ , and  $R_{i,\theta}$  are the distances where the interpolation weight become equal or less than a lower threshold value.

### 3. GAP-FILLING

There are data gaps between the higher tilts in VCP 21 (Fig. 1.1) and VCP 11 (not shown) due to large elevation angle spacings. To fill in the gaps, one option is to increase the smoothing factor  $\kappa_0$  in the weighting function (Eqn.[2.1]) so that the radius of influence becomes large at higher elevations. However, we found that this solution results in arc-shaped discontinuities or concentric circles in the interpolated field when there is horizontally homogeneous echo having strong vertical gradients (e.g., stratiform precipitation). Fig. 3.1 shows a vertical cross-section of reflectivity with a melting layer between 2-4 km. Fig. 3.2a shows a horizontal cross-section of an interpolated reflectivity field at 3.5 km. The high reflectivity arcs seen northwest of the radar are associated with places where the melting layer intercepts the center of radar beams, while the intervening gaps correspond to locations where the bright band intercepts vertical scanning gaps. For grid points in these intervening gaps, the interpolated values are derived from reflectivity in radar bins much higher above or much lower below. This height uncertainty problem has been discussed in previous studies (Howard et al., 1997, Maddox et al., 1999, and Brown et al., 2000). To alleviate this problem, we used an alternate gap-filling scheme in which a horizontal interpolation is performed between the gaps. Fig. 3.2b shows the same horizontal section after the horizontal gap-filling scheme was employed. The discontinuities have been effectively removed.

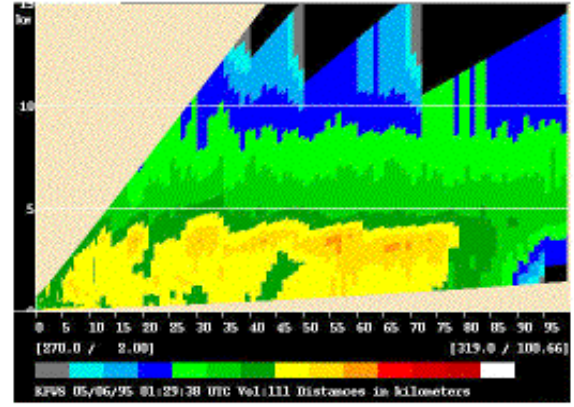


Fig. 3.1 A vertical cross-section of the reflectivity observed by KFWS at 1:30 UTC, May 6, 1995. The cross-section was taken along a line from “A” to “B” in Fig. 3.2a.

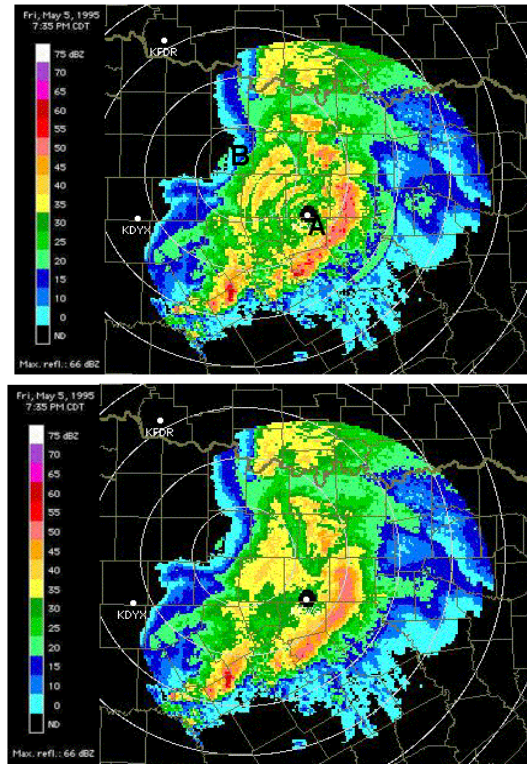


Fig. 3.2 Horizontal sections of the interpolated reflectivity at 3.5 km (msl) before (panel a) and after (panel b) a horizontal gap-filling scheme was employed.

### 4. MOSAIC

The polar-to-Cartesian transformation is performed for each individual radar's volume scan. The remapped reflectivity fields from different radars, which are valid within a given time window (e.g., 10 minutes), are then mosaicked to produce one 3D reflectivity grid using a Cressman type scheme. The mosaic equation is:

$$f_i^m = \frac{\sum_{j=1}^{nrad} w_{i,j} f_{i,j}^a}{\sum_{j=1}^{nrad} w_{i,j}} \quad (4.1)$$



where  $f_{i,j}^a$  represents the interpolated value at the  $i^{\text{th}}$  grid point from the  $j^{\text{th}}$  radar,  $f_j^m$  is the mosaicked reflectivity value at the grid point,  $w_{i,j}$  is the weight given to  $f_{i,j}^a$ . The weight is determined by:

$$w_{i,j} = \frac{R_i^2 - d_{i,j}^2}{R_i^2 + d_{i,j}^2} \quad (4.2)$$

Here  $R_i$  is the influence radius of radar, which is set to 300 km in our scheme, and  $d_{i,j}$  is the distance between the  $j^{\text{th}}$  radar and the  $i^{\text{th}}$  grid point.

Fig. 4.1 shows examples of single radar composite reflectivities from KFWS, KGRK and KTLX, and a mosaicked composite reflectivity. The data are from the Ft. Worth, TX, USA hailstorm case that occurred on May 5-6, 1995. The mosaicked reflectivity provides a more comprehensive depiction of the storm structures and could be more useful for making weather-related decisions than single radar products.

## 5. SUMMARY

A multiple radar reflectivity mosaic scheme has been developed, tested, and employed in real-time operations. An adaptive, Barnes-type filter is used to transform radar reflectivity from their native conical coordinates to Cartesian grids. A Cressman-type scheme is then used for mosaicking multiple radar fields. The advantages of the scheme include its computational efficiency and the retention of high-resolution meteorological information. The multiple radar reflectivity mosaic has been tested in several applications including a real-time regional reflectivity display, an aviation control display and a radar climatological study.

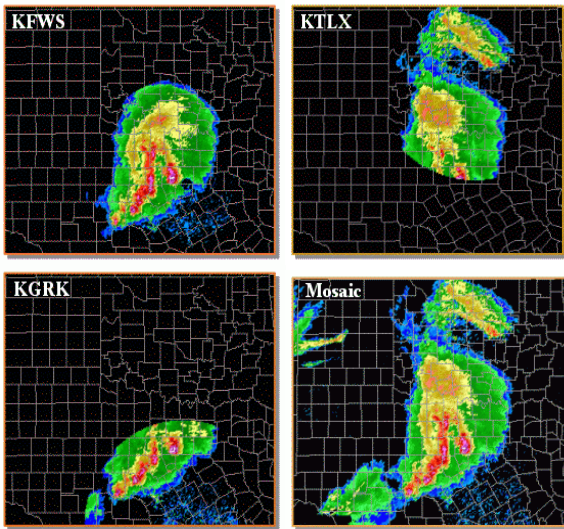


Fig. 4.1 Composite reflectivities from KFWS, KTLX, KGRK radars and from a 3D reflectivity mosaic using 7 radars (the aforementioned 3 plus KAMA, KLBB and KEMX). The images were valid at 2330 UTC on May 5, 1995.

## 6. REFERENCES

Available upon request.

- Askelson M.A., J-P. Aubagnac, and J.M. Straka, 2000: An adaptation of the Barnes filter applied to the objective analysis of radar data. *MWR*, **128**, 3050-3082.
- Brown, R. A., V. T. Wood, and D. Sirmans, 2000: Improved WSR-88D scanning strategies for convective storms. *Wea. Forecasting*, **15**, 208-220.
- Howard, K. W., J. J. Gourley, and R. A. Maddox, 1997: Uncertainties in WSR-88D measurements and their impacts on monitoring thunderstorm life cycles. *Wea. Forecasting*, **12**, 166-174.
- Maddox, R. A., D. S. Zaras, P. L. Mackeen, J. J. Gourley, R. Rabin, and K. W. Howard, 1999: Echo height measurements with the WSR-88D: use of data from one versus two radars. *Wea. Forecasting*, **14**, 455-460.
- Trapp, R. J. and C. A. Doswell, 2000: Radar data objective analysis. *JTECH*, **17**, 105-120.